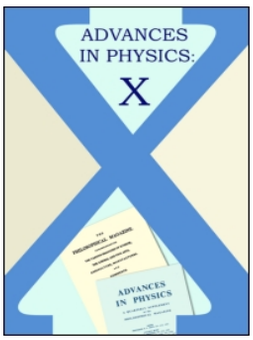

Advances in Physics: X

ISSN: (Print) 2374-6149 (Online) Journal homepage: http://www.tandfonline.com/loi/tapx20

IR spectroscopy applied to metal oxide surfaces: adsorbate vibrations and beyond

Chengwu Yang & Christof Wöll

To cite this article: Chengwu Yang & Christof Wöll (2017) IR spectroscopy applied to metal oxide surfaces: adsorbate vibrations and beyond, Advances in Physics: X, 2:2, 373-408, DOI: 10.1080/23746149.2017.1296372

To link to this article: http://dx.doi.org/10.1080/23746149.2017.1296372

Published online: 28 Mar 2017.

ADVANCES IN PHYSICS: X, 2017
VOL. 2, NO. 2, 373–408
http://dx.doi.org/10.1080/23746149.2017.1296372

Taylor & Francis
Taylor & Francis Group

REVIEW ARTICLE

OPEN ACCESS

IR spectroscopy applied to metal oxide surfaces: adsorbate vibrations and beyond

Chengwu Yang and Christof Wöll

Institute of Functional Interfaces, Karlsruhe Institute of Technology, Karlsruhe, Germany

ABSTRACT

Metal oxides are among the technologically most important materials. Almost all metals are covered by one oxide layer under ambient conditions. The characterization of oxide surface properties, therefore, is still attracting an increasing amount of attention in surface science. A challenge is provided by the fact that these materials cannot be studied with standard techniques in a straightforward fashion. In this review, we summarize recent results obtained by IR-spectroscopy applied in a reflection-geometry to macroscopic oxide monocrystals. These results provide new insights in the adsorption and subsequent reactions and photoreactions of molecules on these highly interesting, very complex class of materials. In addition, the IR-spectroscopy can also be used to probe photophysical properties, e.g. the generation and decay of electron or hole polarons.

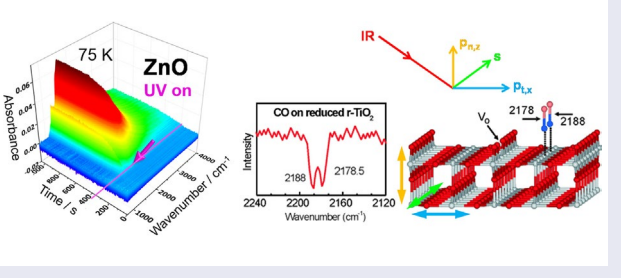

ARTICLE HISTORY
Received 9 December 2016
Accepted 13 February 2017

KEYWORDS
Oxides; IR-spectroscopy; molecular vibrations; polarons; photochemistry

PACS
33.20.Ea (Infrared spectra); 68.43.-h (Chemisorption/physisorption: adsorbates on surfaces); 82.50.-m (Photochemistry); 71.38.-k Polarons and electron-phonon interactions

1. Introduction

Metal oxides represent one of the most important and widely employed classes of technologically relevant materials with applications in catalysis [1], gas sensors [2], photochemistry [3], optoelectronics [4], and photovoltaics [5]. These materials are also relevant in completely different areas, e.g. for biomedical applications [6,7]. Here, the biocompatibility of metal implants is enhanced by the properties of their

CONTACT Christof Wöll christof.woell@kit.edu

oxide layers naturally formed in the presence of oxygen, e.g. as a passivation layer to protect the implant from corrosion in body fluid [8]. Furthermore, they are omnipresent since – with the exception of gold – under ambient conditions all metals are covered by an oxide. The interaction of molecules with oxides is thus not only highly relevant for heterogeneous catalysis, but also for other phenomena, including corrosion, lubrication, and adhesion of polymers (paints, adhesives) to oxides. Therefore, a thorough investigation of the interaction of molecules with oxide surfaces, including determination of binding strengths, chemical reactions following adsorption, etc., is urgently required.

In the case of clean metals, the so-called surface science approach has been very successful with regard to understanding chemical properties of surfaces. The great success of this approach is based on a huge arsenal of surface-sensitive techniques developed during the past 60 years, which has provided detailed insights into the fundamentals of molecule-substrate interactions [9,10]. For oxides, on the other hand, only since the mid-1980s, studies have blossomed on planar model surfaces of metal oxides. Today, the amount of information on molecule-substrate interactions available for these binary compounds [11,12] is much smaller than in case of metals. This lack of information does not reflect missing interest, but rather results from the larger complexity and, more importantly, from the low electrical conductivity of these dielectric materials. Charging problems occurring for oxidic substrates severely hamper the application of various techniques using charged-particle beams, including the different variants of photoelectron spectroscopies. In addition, the application of scanning tunneling microscopy, or STM, to oxides works well only for a few oxides in their bulk form (e.g. TiO_2 [13]).

Infrared (IR) spectroscopy has been widely used for the characterization of molecular adsorbates on metals, both on monocrystalline substrates [14–16] as well as for metal particles [17,18]. Infrared reflection absorption spectroscopy (IRRAS) is a variant of IR-spectroscopy suited for the investigation of adsorbates on planar model surfaces. This method was developed in the 1960s and has proved to be a particularly powerful research tool for the study of adsorbed layers on metal surfaces. In fact, the success of IRRAS has contributed substantially to the identification of fundamental principles governing the surface chemistry of metals [19,20].

For oxides, the situation is quite different. Applications of IRRAS to such dielectric substrates are extremely scarce. Before 2007, there was only one paper presenting IRRAS data for a molecular adsorbate on a monocrystalline oxide surface [21], compared to >500 papers for IRRAS on metal single-crystal surfaces. Obviously, the reason for this lack of information cannot be related to the charging problems alluded to above, which do not affect IR spectroscopy. Instead, for dielectrics the intensity of IR-light reflected from the surface in the specular direction is generally reduced to a level which makes detection of the small changes in absorbance caused by excitations of adsorbate vibrations a difficult task. Compared to metals, sensitivities (i.e. $\Delta R = R_0 - R_F$, R_0 and R_F are the reflectivities of the clean substrate

and the film-covered substrate, respectively) are typically down by one to two orders of magnitude [22].

The analysis of IRRAS data obtained for oxidic substrates is considerably more demanding than for metals. IRRAS applied to metals is governed by the so-called surface-selection rule [20,23]. Since the screening by the charge carriers in the substrate causes the surface electric field to be perpendicular to the surface, only vibrations with a nonzero component of the transition dipole moments (TDM) oriented perpendicular to the substrate can cause signatures in the IR-spectra. In addition, for metal substrates, absorbance bands caused by excitation of adsorbate vibrations are always positive (i.e. excitation of the vibration leads to a decrease in reflected intensity). For dielectrics, as a result of the absence of a large density of conduction band electrons, the component of the incident light parallel to the surface is not screened (as in the case of metals), and the surface selection rule governing IRRAS for metals does not apply any longer. For dielectrics, in general, also vibrations with TDMs oriented parallel to the surface can be probed. Consequently, for oxides, adsorbate vibrations can be detected with s- and p-polarized light, allowing probing vibrations parallel to the surface as well as perpendicular to it. Finally, the excitation of vibrational bands by the incident IR-light can cause intensity increases as well as decreases in the reflected intensity, i.e. negative as well as positive vibrations bands can be observed.

The technical difficulties in applying IR to oxides discussed above have motivated the research on metal oxide thin films grown on appropriate metal substrates. Because of the excellent reflectivity of the supporting metal substrates, for these thin oxide layers IRRAS can be applied in a straightforward fashion. In fact, the investigation of oxide thin films has been developed in a well-established, alternative method to investigate vibrational properties of adsorbates on oxides by IR spectroscopy [24,25]. Despite the huge success of this approach, however, a controversy has started on the question whether structural and electronic properties of oxide thin films are the same as for bulk oxides or whether in particular, thin oxide films (thicknesses < 10 nm) are affected by the metal support [26]. There are a number of cases where pronounced differences, e.g. originating from charge transfer, between oxide thin films and their bulk counterparts have been reported [27–34]. In addition, for investigations regarding photocatalytic and photophysical properties of oxides, thin oxide films are not well suited because of photoelectrons originating from the metal support might affect the experimental results.

In view of these problems, after the pioneering work of Hayden and co-workers [21], a few groups have started to optimize technical equipment in order to allow for IRRAS studies of adsorbed molecular monolayers also on oxide bulk single crystals [35–62]. In this review, we briefly present the results of such IRRAS studies for small adsorbates bound to monocrystalline metal oxide surfaces carried out by the group at Karlsruher Institut für Technologie (KIT). A particular emphasis will be on the adsorption of carbon monoxide (CO), which is frequently used as a probe molecule [63] also for oxide powder samples. In addition to IR spectroscopy

applied to molecular adsorbates, we will also briefly discuss the application of IR spectroscopy to investigate photophysical properties of oxide surfaces. In such experiments, time-resolved IR spectra are recorded after illumination of the oxide substrate with UV light. These spectra yield information on polarons (quasiparticles consisting of electrons or holes dressed by their surrounding lattice distortion) within the oxide which are created by the dissociation of photogenerated excitons.

The adsorption of CO on metal oxide surfaces is not only governed by chemical interactions as on metal surfaces, but also by electrostatic interactions with the electric field generated by the surface metal cations and oxygen anions. In contrast to CO adsorption on metals, where generally a red-shift of adsorbed CO is seen, these interactions lead to a blue-shift of the CO stretching frequency with respect to the CO gas phase value. A more thorough analysis yields that indeed the electrostatic interactions (Stark effect) are one of the main reasons for such blue shifts [64].

Below, we will present high-quality IRRAS results recorded after adsorption of CO on TiO_2, ZnO, and CeO_2 monocrystalline surfaces, together with a detailed discussion. We will also present the results of an IRRAS study of carbon dioxide (CO_2) adsorption on ZnO(1 0 $\bar{1}$ 0). This is an interesting example to demonstrate the particular aspects of IR spectroscopy of molecular vibrations at oxide surfaces. In contrast to the case of adsorbates on metal surfaces, the availability of polarization- and azimuth-resolved IR spectra on oxides allows for a direct determination of the adsorbate geometry.

2. Experimental

2.1. Ultrahigh vacuum apparatuses

The *in situ* Fourier-transform IRRAS experiments were performed using two state-of-the-art ultrahigh vacuum (UHV) apparatuses, both manufactured by Prevac (Rogów, Poland), at Karlsruhe and Bochum, respectively. The KIT setup, also referred to as THEO, is based on an earlier apparatus operated at Ruhr-Universität Bochum [37]. THEO is dedicated to the spectroscopic characterization of oxides; different scattering geometries allow to investigate macroscopic single crystals as well as powders [65]. The innovative design allows combining several surface-sensitive techniques in one apparatus. In contrast to most other designs, THEO uses a single-frame set-up where the IR source, the detector as well as the interference line are all attached to the same solid, single frame. This approach reduces differential vibrations between these components. Basically, a specifically designed UHV chamber (fitted with a sample holder which allows sample temperatures as low as 60 K) is inserted into the sample compartment of a conventional FTIR spectrometer (Bruker VERTEX 80v) to form a compact connection and thereby avoiding vibrations of the detector with regard to the IR interferometer.

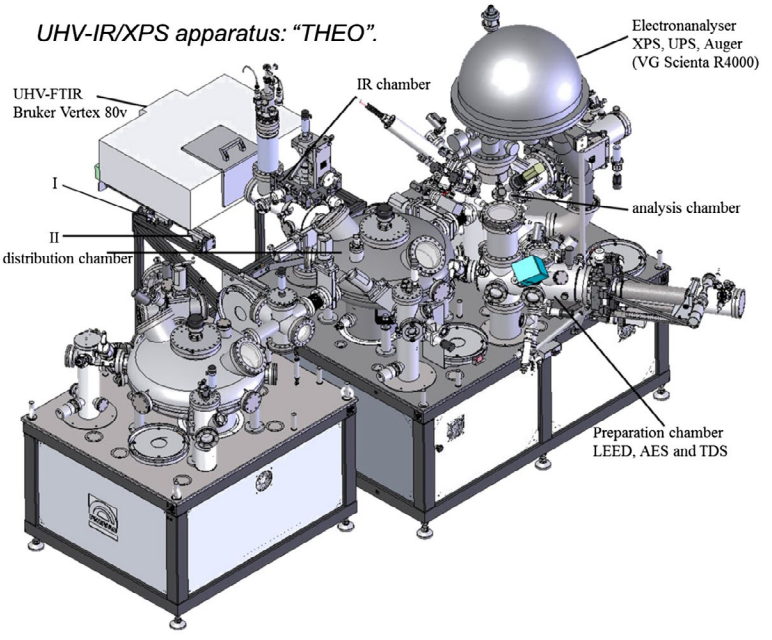

Figure 1. Technical drawing of UHV apparatus THEO.

The UHV apparatus THEO (cf. Figure 1) consists of two big oblate ellipsoidal distribution chambers, which are connected together by a reorientation chamber, and multifunctional chambers, such as load-lock, preparation, infrared, storage magazine, and analysis chamber, are also attached. The analysis and preparation chamber allow to carry out additional sample characterizations using other surface-sensitive techniques, including low energy electron diffraction (LEED), X-ray photoelectron spectroscopy (XPS), ultraviolet photoelectron spectroscopy, Auger electron spectroscopy, and thermal desorption spectroscopy (TDS).

2.2. UHV-IRRAS

The heart of the UHV equipment is the IR chamber. The unique configuration consists of an UHV chamber inserted into a (slightly modified) commercial spectrometer (Bruker VERTEX 80v). The IR light transmitted into the UHV-IR chamber through differentially pumped KBr windows. The inner part of the spectrometer (containing e.g. the interference line) is evacuated to below 2 mbar. The differentially pumped windows between the UHV chamber and spectrometer are sealed by Viton O-rings and can be evacuated to a vacuum of better than 1×10^{-6} mbar. Thus, the entire optical path is kept in vacuum/UHV to avoid any absorption from atmospheric moisture and other gas species (e.g. CO_2). This particular set-up, inserting the UHV-chamber in the commercial set-up, allows for the acquisition of spectra at grazing incidence (80°) of sample substrates kept

under UHV conditions without introducing any new optical elements in the path of the infrared light. This fact is considered crucial for the high performance of this IR/UHV combination and guarantees high-quality IR data with high sensitivity and long-term stability, requirements which are needed to be fulfilled for the detection of the very weak IR bands on monocrystalline oxide surfaces. The FTIR spectrometer is equipped with a polarizer, which makes it possible to measure with s- and p-polarized light. The adsorption geometry of molecules on metal oxide surfaces thus can be better examined in particular, as on these surfaces the surface selection rule, unlike metals, does not apply [43], since screening by the substrate leads to a surface electric field on metals that are oriented strictly perpendicular to the surface plane. As such, IRRAS applied to metals is only sensitive to the normal component of any vibrational band. It should be noted that the innovative design of this apparatus allows not only to record IRRAS data at grazing-incidence on well-defined oxide single-crystal surfaces, but makes it also possible to carry out IR measurements in transmission with oxide powder particles. For the latter, the scattering geometry is changed from reflection to transmission by repositioning the detector inside the VERTEX 80v spectrometer, i.e. again without including additional elements into the optical path.

3. TiO_2

TiO_2 is a prototypical material used in catalysis [66,67], photocatalysis [68], and Grätzel solar cells [69]. It also has promising properties for use in electronics as a transparent conductive oxide [70,71] or a memristor [72]. Furthermore, medical implants (e.g. artificial hips) are often made from Ti, and the biocompatibility of the TiO_2 surface layer therefore is highly relevant for the proper function of such artificial body parts. TiO_2 has two main polymorphs relevant for industrial applications: rutile and anatase. The former has received the most scientific attention. Nonetheless, the metastable anatase is believed to be the more catalytically active phase and is therefore preferred in most industrial applications.

3.1. CO/rutile-TiO_2(1 1 0) [40]

The IRRAS data shown in Figure 2 demonstrate that on a fully oxidized rutile-TiO_2(1 1 0) surface with a low defect density, only a single band at 2188 cm^{-1} is observed upon exposure to CO at 110 K. Note the negative sign of the vibrational band, a characteristic feature which is only present in case of oxides. On metal substrates, the intensity of reflected light always decreases upon excitation of a vibration, thus only positive bands are seen. This frequency is 45 cm^{-1} higher than that observed for the gas phase CO (2143 cm^{-1}), which is in complete accord with previous results of electron energy loss spectroscopy and theoretical studies for CO adsorbed on the same substrate [73]. The blue-shift of stretching mode of adsorbed CO molecules with respect to the gas phase is mainly due to the

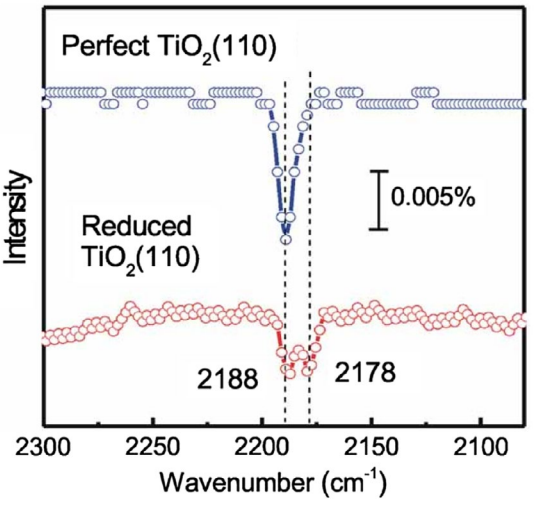

Figure 2. IRRAS data for CO adsorbed on perfect and reduced rutile-TiO_2(1 1 0) surfaces at 110 K (the vertical axis represents absorbance) [40]. Source: Copyright © 2012 John Wiley & Sons.

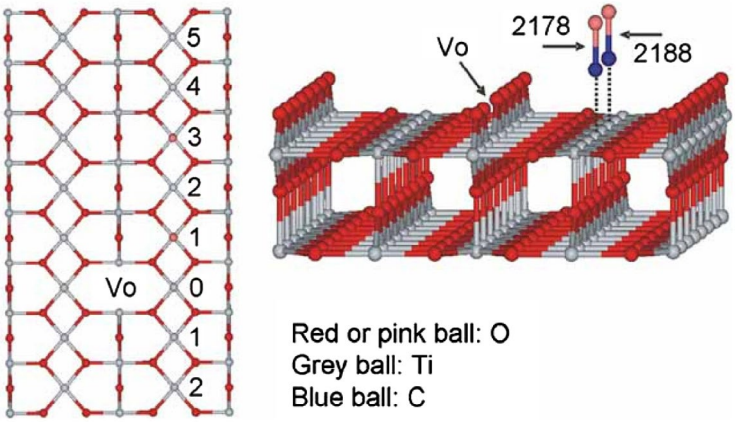

Figure 3. Ball-and-stick model of the rutile-TiO_2(1 1 0) surface [40]. The CO species adsorbed at different Ti sites (labeled 0–5) are also depicted. Source: Copyright © 2012 John Wiley & Sons.

electrostatic polarization of the CO dipole by the metal cation (Stark effect) and Pauli repulsion occurring when the molecule vibrates against a rigid surface (wall effect) [74]. When the TiO_2 surface was reduced either by controlled slightly sputtering or annealing under UHV conditions, a second CO band appeared at 2178 cm^{-1}. In line with a recent STM study on rutile-TiO_2(1 1 0) by Zhao et al. [75], the reduction-induced band at 2178 cm^{-1} is assigned to CO adsorbed at Ti cations located in the vicinity of an oxygen vacancy (i.e. site 1 indicated in Figure 3), whereas the band at 2188 cm^{-1} is assigned to CO bound to regular sites of the surface (sites 2–5 in Figure 3). In order to corroborate the assignment of the band at 2178 cm^{-1} to defect-related adsorption sites, we blocked the Ti cation

sites close to the oxygen vacancies by exposing the substrates to small amount of O_2 at 110 K. As expected, in the IR spectra recorded after such substrates pretreated with O_2 were exposed to CO at 110 K, the band at 2178 cm^{-1} was found to be strongly reduced relative to the band at 2188 cm^{-1}. Using a different UHV-IRRAS apparatus, Petrik and Kimmel [51] studied the same system. Using s- and p-polarized IR light incident along the [0 0 1] and [1 $\bar{1}$ 0] azimuths, they were able to obtain detailed information on the adsorption geometry of CO as a function of the CO coverage, θ_{CO}. The results indicated that for $\theta_{CO} \leq 1$ monolayer (ML), CO adsorbs oriented perpendicular to the surface at fivefold Ti cation sites. For $1 < \theta_{CO} \leq 1.5$ ML, the bonding geometry of the CO adsorbed at fivefold coordinated Ti cation sites is unchanged, whereas the additional CO molecules adsorb at surface bridging O anion sites parallel to the surface and parallel to the [1 $\bar{1}$ 0] azimuth.

3.2. CO/anatase-TiO_2(1 0 1) [46]

In contrast to rutile (which is considered to be the best-understood oxide as far as surface properties are concerned [13]), much less is known about the metastable anatase. However, in many applications, in particular in photochemistry, anatase outperforms rutile. It is therefore mandatory to study the properties of this titania polymorph as well. The IRRAS results of CO adsorption on anatase-TiO_2(1 0 1) are shown in Figure 4. For the spectra displayed in the top panel (Figure 4(a)), the low reduction state of the substrate was confirmed by the absence of the Ti^{3+} shoulder in the Ti2p XP spectra [13]. After characterization, the sample was exposed to CO at 95 K resulting in different coverages. At low coverage, a single peak at 2185 cm^{-1} was detected in the CO stretching region (Figure 4(a)), which shifts to the lower frequencies to 2181 cm^{-1} upon increasing the CO coverage close to 1 monolayer (ML). Figure 4(c) shows the IR data acquired with p- and s-polarized light. In spectra recorded for p-polarized light incident along both, the [0 1 0] and [$\bar{1}$ 0 1] directions, only an single negative CO band at 2181 cm^{-1} was observed, indicating that the dynamic dipole moment of the CO stretching vibration interacts mainly with the component of the p-polarized light normal to the surface (the orientation of the s- and p-polarized components for the incident IR light is depicted in Figure 20) [43]. No vibrational band was observed in spectra recorded with s-polarized light (Figure 4(c)). For s-polarized light, the electric field vector is oriented parallel to the surface and perpendicular to the incidence plane (cf. Figure 20). These observations indicate that the adsorbed CO adopts an orientation nearly perpendicular to the surface.

IRRAS data for samples which were subjected to many sputter-annealing cycles so as to increase the reduction extent also show only a single CO band at 2181 cm^{-1} (Figure 4(b)). This behavior is different from the case of rutile-TiO_2(1 1 0) [40] or CeO_2(1 1 1) [42], where surface reduction resulted in the appearance of a secondary CO stretching peak either red-shifted or blue-shifted by about 10 cm^{-1}

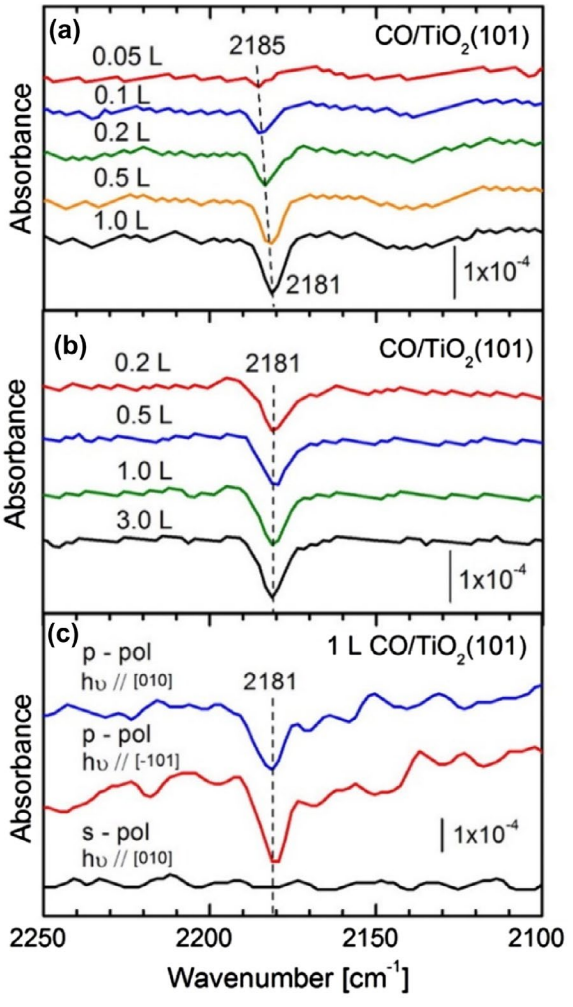

Figure 4. IRRAS data of different doses of CO adsorbed at 95 K on (a) stoichiometric and (b) reduced anatase (1 0 1) surfaces with non-polarized light; (c) IRRAS data of 1 L CO adsorbed at 70 K on stoichiometric TiO_2(1 0 1) with p-polarized light along [0 1 0] and [$\bar{1}$ 0 1] and s-polarized light along the [0 1 0] azimuth [46]. Source: Copyright © 2015 American Chemical Society.

relative to the vibrational band observed on their stoichiometric counterparts. On anatase-TiO_2(1 0 1), distinct additional CO vibrational peaks or strongly bound CO species were not detected (see Figure 4(b)). The measurements were repeated several times on two different anatase mineral samples, with very similar results. The CO stretching frequency at 2181 cm^{-1} is assigned to CO adsorbed on fivefold coordinated Ti cations (Figure 5), independent of the reduction state. We attributed the observed behavior to the lack of O-vacancies within the anatase top layer. By comparing the results of a thorough theoretical analysis, our data also indicate that single subsurface oxygen vacancies directly below the anatase (1 0 1) surface (i.e. in the second layer) must be a rather rare species [46].

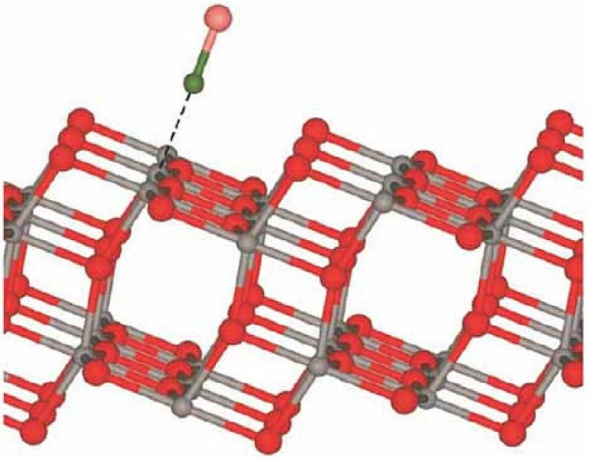

Figure 5. Ball-and-stick models of anatase-TiO_2(1 0 1) [39]. Red or pink ball: O; gray ball: Ti; green ball: C. Source: Copyright © 2011 American Physical Society.

3.3. Photocatalytic CO oxidation on rutile and anatase [36,39]

TiO_2 has been the most intensively studied semiconductor photocatalyst so far due to its high activity under UV irradiation and extraordinary stability against photocorrosion [66–68,76–78]. However, previously reported studies on the photocatalytic properties of TiO_2 were almost exclusively carried out for samples in powder form. Owing to the usual ill-defined surface structure of powder particles, it was very difficult to elucidate fundamental issues related to photochemistry at TiO_2. In particular, the origin of the higher photocatalytic efficiency of anatase as compared to rutile is not well understood and remains a matter of debate. Here, we discuss the results of a recent surface science study on well-defined rutile and anatase monocrystalline TiO_2 surfaces using IRRAS. The high-quality IR data allowed for new insights into the surface photochemistry of these two different TiO_2 polymorphs.

The IR spectrum A in Figure 6(a) obtained after exposing the clean rutile-TiO_2(1 1 0) surface to 10^{-7} mbar of CO at 110 K clearly shows a distinct peak at 2183 cm^{-1}. After evacuating the UHV chamber back to 10^{-10} mbar, the CO peak slightly shifts to higher frequencies, 2190 cm^{-1}, and decreases by ~25% in intensity (Figure 6(a), spectrum B). In a test experiment, the system (rutile-TiO_2(1 1 0) covered with CO) was illuminated with UV light (3.2 eV) in the absence of gas phase oxygen (Figure 6(a), spectrum B). The signals are virtually unchanged, in accord with expectations, since photodesorption of CO only occurs for higher photon energies (above 4.3 eV) [79].

When the exposure to UV photons was repeated in the presence of molecular oxygen (10^{-7} mbar), a continuous decrease in the intensity of the CO vibrational peak with irradiation time was observed (Figure 6(a), spectra C–F). Since no decrease in the CO peak was seen in the absence of O_2, this observation implies

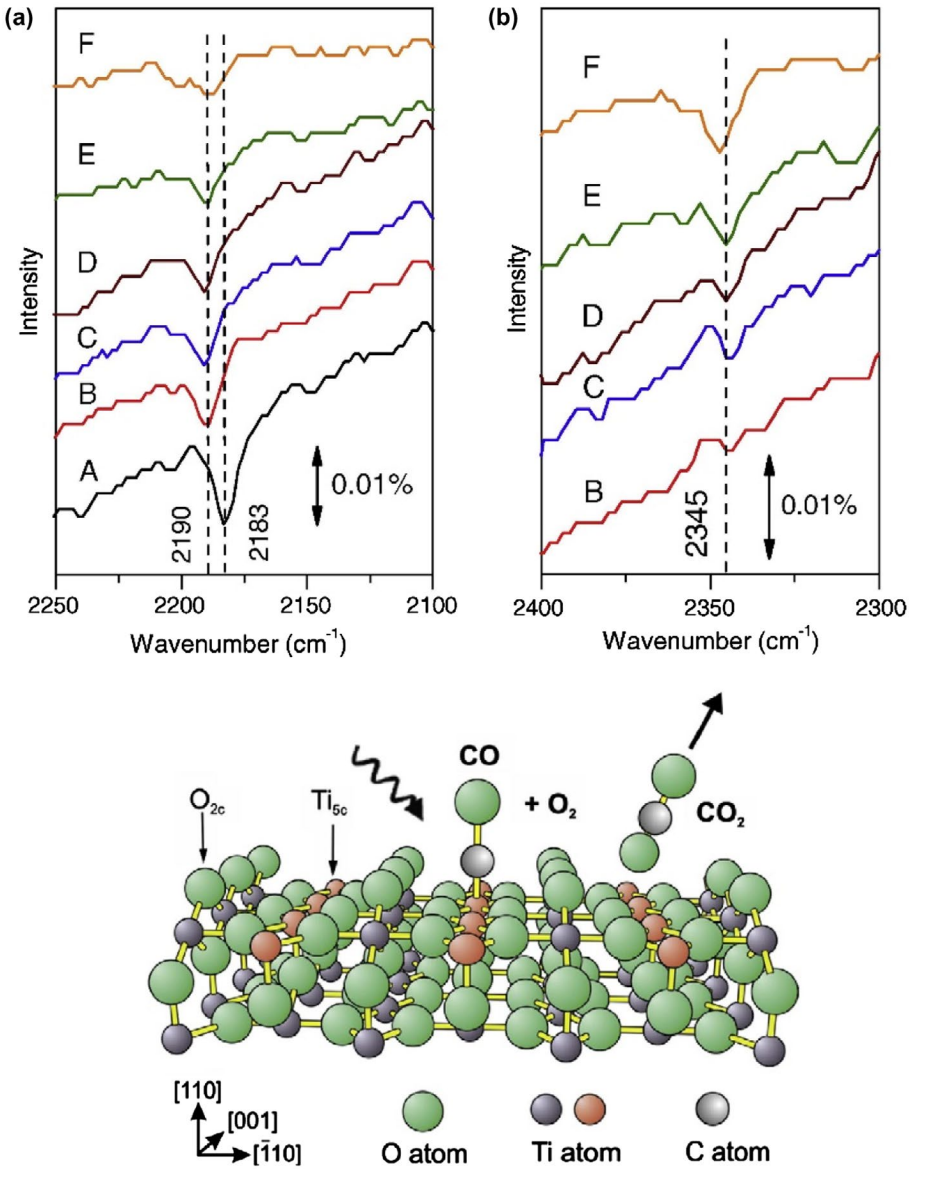

Figure 6. Top: Panel (a). IRRAS data of CO on TiO_2(1 1 0) single crystal surface at 110 K. A, $P_{CO} = 10^{-7}$ mbar; B, after evacuation to 10^{-10} mbar; C, after exposing (B) for 8 min to UV light (3.2 eV) in presence of 10^{-7} mbar of O_2; D, after a total exposure of 24 min to UV light; E, after a total exposure to 40 min to UV light; F, after a total exposure to 56 min to UV light (the vertical axis represents absorbance) [36]. Panel (b). The CO_2 region; labels correspond to those of panel (a). Bottom: a side view of the TiO_2(1 1 0) surface and adsorbed CO molecules on top of Ti atoms (red) fivefold coordinated to oxygen atoms (green). Source: Copyright © 2008 Elsevier.

a reaction of CO with activated O_2 to yield CO_2, in accord with previous work where the photocatalytic production of CO_2 was detected under such conditions [80]. In the present measurements, some fraction of CO_2 produced by the reaction actually remains at the surface, as shown by the appearance of a new band at

2345 cm^{-1} being characteristic of physisorbed CO_2 (Figure 6(b)). Note that the desorption temperature of physisorbed CO_2 on this surface amounts to ~140 K [81]. The occurrence of this vibrational band is a nice, direct proof for this photoreaction producing CO_2.

According to Yates and co-workers [80], the photocatalytic formation of CO_2 is brought about by activation of O_2 molecules through electron-hole (e-h) pairs generated within the TiO_2 by absorption of UV photons [80,82]. The fact that characteristic vibrational features of formate species ($HCOO_{ad}$) or carbonates (CO_{3ad}) could not be observed in the IRRAS data indicates the absence of a long-lived, chemically distinct intermediate species. The capability of IRRAS to detect formate species, a possible reaction intermediate, has been demonstrated by the observation of characteristic IR-bands after exposure of rutile-TiO_2(1 1 0) to gas phase formic acid [21]. In earlier work, the products of this photocatalytic process could be studied only in the gas phase [82], thus prohibiting a direct observation of surface intermediates. These IRRAS observation therefore provide the first direct evidence that the reaction of adsorbed CO proceeds most likely with either O-adatoms or activated O_2 species, leading directly to CO_2-formation. In previous works, an intermediate state corresponding to an O–O–CO complex was proposed for CO photo-oxidation on rutile TiO_2(1 1 0) theoretically [83–85] and experimentally [86]. Note, however, that for such an O–O–CO intermediate with a relatively long distance between O_2 and CO [84], we expect the CO stretch frequency to be substantially different from CO adsorbed on the pristine rutile surface. Since no new IR signals were observed in the IRRAS experiments, we feel that a long-lived O–O–CO intermediate under our measurement conditions can be excluded. A metastable, short-lived intermediate, however, would be consistent with the IRRAS data. Moreover, the IRRAS data indicate that the CO_2 produced from adsorbed CO by photo-oxidation is only weakly physisorbed on the surface and does not further react with surface bridging oxygen anions to form new chemical species (such as carbonate).

The different photocatalytic efficiency of rutile and anatase as regards to CO photo-oxidation is demonstrated by the IRRAS data shown in Figure 7. Exposure of anatase-TiO_2(1 0 1) to CO at 100 K leads to the appearance of an IR peak at 2180 cm^{-1}. When the TiO_2(1 0 1) surface pre-covered with CO is further exposed to molecular oxygen under UV illumination with photon energy of 3.40 eV, the photo-induced oxidation of CO occurs as indicated by the gradual decrease of the CO band intensity. This photoreaction was further confirmed by a new peak growing simultaneously at 2340 cm^{-1}, which is attributed to physisorbed CO_2. The different sign of the two peaks at 2180 and 2340 cm^{-1} results from the different orientation of the adsorbed species, CO and CO_2, relative to the substrate. Based on the IR data shown in Figure 7(b), the photoreaction cross section Q is determined to 2.0×10^{-17} cm^2 for anatase, an order of magnitude larger than

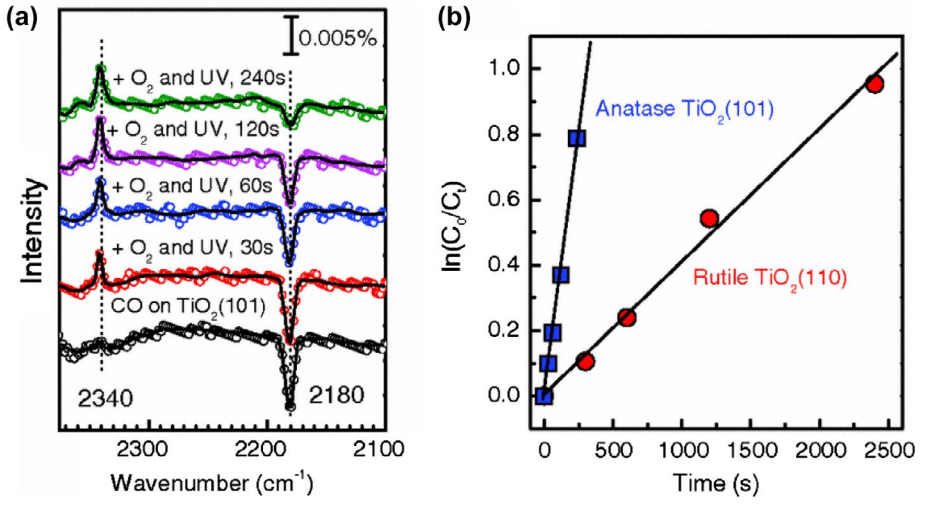

Figure 7. Photo-oxidation of CO on TiO_2 monitored by IRRAS (the vertical axis represents absorbance) [39]. (a) IRRAS data of CO and CO_2 during photo-induced CO oxidation reaction on the anatase-TiO_2(1 0 1) single crystal surface at 100 K. The sample was first exposed to CO (10^{-7} mbar) and then exposed to O_2 (10^{-7} mbar) and UV light (3.4 eV, 2×10^{14} photons/(cm^2 s)) for different times. (b) Comparison of the reaction cross section Q of CO photo-oxidaton on rutile-TiO_2(1 1 0) and anatase-TiO_2(1 0 1). Plotted is the $\ln(C_0/C_t)$ as a function of the UV irradiation time. C_0 is the initial CO coverage before UV irradiation, and C_t is the CO coverage after irradiation at time t. The blue squares are the data for CO on anatase-TiO_2(1 0 1) as shown in Figure 7(a). The red circles denote data for CO on rutile-TiO_2(1 1 0). Source: Copyright © 2011 American Physical Society.

that for the different titantia polymorph, rutile (2.0×10^{-18} cm^2). For both rutile-TiO_2(1 1 0) and anatase-TiO_2(1 0 1) surfaces, CO oxidation with surface bridging oxygen anions in the presence of UV could not be detected. Also, dark reaction ($CO + O_2$) does not take place on either of the substrates.

We found that this significant difference in photocatalytic performance between well-defined anatase and rutile surfaces could not be attributed to the density of surface defects or the nature of CO interaction with substrates. Contactless transient photoconductance measurements [39] revealed that the lifetime of photo-excited e-h pairs in anatase (>10 ns) is about an order of magnitude longer than that for rutile (<1 ns). This difference in the lifetime of bulk e-h pairs for the two TiO_2 polymorphs should be responsible for the larger photocatalytic efficiency of anatase than rutile. The longer lifetime of e-h pairs in anatase facilitates the translocation of the photo-generated electrons and holds from bulk to the surface, where the photochemical reactions take place. The large difference in e-h pair lifetime between anatase and rutile could be due to their different band structures. Whereas rutile has probably a direct band-gap, anatase exhibits a special indirect band-gap [87]. As a result, the recombination of the photo-generated e-h pairs in anatase will be largely reduced, thus increasing the e-h lifetime.

3.4. IR-signatures of photo-generated charge carriers in TiO_2 [88]

In order to investigate the IR-signatures of charge carriers (either electrons in the conduction band or holes in the valence band), IR spectra were recorded for rutile-TiO_2(1 1 0) surfaces before and after illumination with UV light are shown in Figure 8. In these differences in spectra (a spectrum recorded before UV exposure is subtracted from the spectrum recorded after UV exposure), we clearly observe a main feature localized at 910 cm^{-1} along with two additional features at 1205 and 1375 cm^{-1}. The observation of such UV-induced features in TiO_2 has been reported previously for titania powders by Yates and co-workers [89–95]. However, in this earlier powder data, the sharper features at 1205 and 1375 cm^{-1} could not be identified. Interestingly, these IR-bands, which we attribute to excitations of charge carriers resulting from photon absorption, can also be observed after exposing both powder particles and TiO_2 single-crystal surfaces to hydrogen

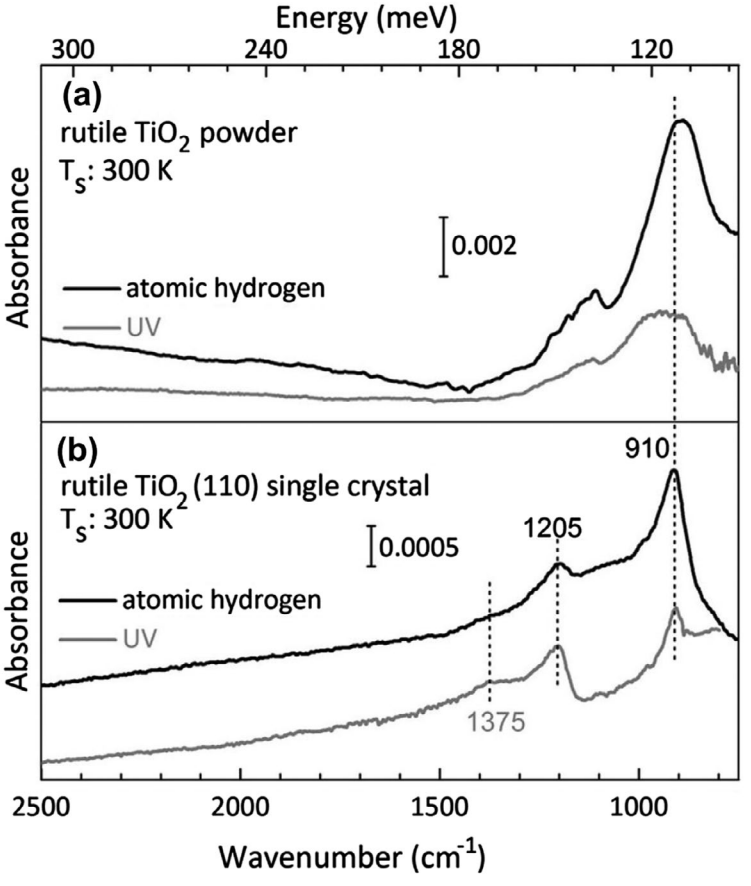

Figure 8. Recorded after the exposure of (a) powders and (b) a rutile-TiO_2(1 1 0) single crystal to UV-light or atomic H [88]. The difference spectra shown were obtained by subtracting a background spectrum for the pristine sample recorded directly before filling the trap states from the raw data. Source: Copyright © 2014 Nature Publishing Group.

atoms generated by thermal dissociation of hydrogen molecules. According to previously proposed mechanisms, the electrons bound to these hydrogen atoms incorporated into the bulk TiO_2 have only small binding energies, and can easily be transferred to the conduction band, thus resulting in an effective n-doping of this large band-gap semiconductor. From the similarity of the results observed after the UV-exposure and the hydrogen atoms exposure, we conclude that the features seen in the infrared data at 910, 1205, and 1375 cm^{-1} are actually related to electrons in the conduction band. In the case of the UV-exposure, they are generated by dissociation of the excitons resulting from the photoabsorption process (photon doping), whereas in the latter case the electrons result from the incorporated H-atoms (chemical doping). In our previous report [88] we proposed that the signatures in the infrared data are actually due to an excitation of electrons bound within polaron traps. At present, we feel that this explanation is likely to be incorrect. Unfortunately, the theoretical description of polarons in oxidic materials is rather complicated and, despite substantial effort, the reported theoretical values for the binding energies differ substantially [88,96,97]. At present, it is also conceivable that the excitations seen in the IR data are actually related to small polarons localized in the vicinity of defects. The nature and position of these defects, however, is still unclear.

4. ZnO

Today, in terms of industrial benefit, ZnO is one of the most important oxides. Methanol, the third most-important chemical product of chemical industry, is produced from syngas (a mixture of CO, H_2, and often some CO_2) using a Cu/ZnO/Al_2O_3 catalyst, where small Cu particles are activated by interaction with a ZnO substrate [98].

4.1. *CO/ZnO*(1 0 $\bar{1}$ 0) *[48]*

It is well known that the nonpolar, mixed-terminated ZnO(1 0 $\bar{1}$ 0) surface is energetically the most favorable surface of this interesting oxide, and studies on ZnO powder samples using electron microscopy have shown that among the different faces exposed by ZnO nanoparticles, the (1 0 $\bar{1}$ 0) orientation plays the most important role [99]. In the present experiments, the ZnO(1 0 $\bar{1}$ 0) sample was cooled down to 60 K and then exposed to CO to achieve saturation coverage (1 ML). The corresponding IRRA spectra recorded with p-polarized light incident along the [1 $\bar{2}$ 1 0] azimuth are shown in Figure 9. Also, an IR spectrum recorded for the bare ZnO (black curve) is displayed for comparison. We observed an intense IR band at 2169 cm^{-1}, which is assigned to the stretching vibration of CO molecules bound to the surface Zn^{2+} cations. This frequency, exhibiting a blue-shift of 26 cm^{-1} compared to the gas phase value (2143 cm^{-1}), is in good agreement with the results obtained for CO adsorption on ZnO nanoparticles [100,101].

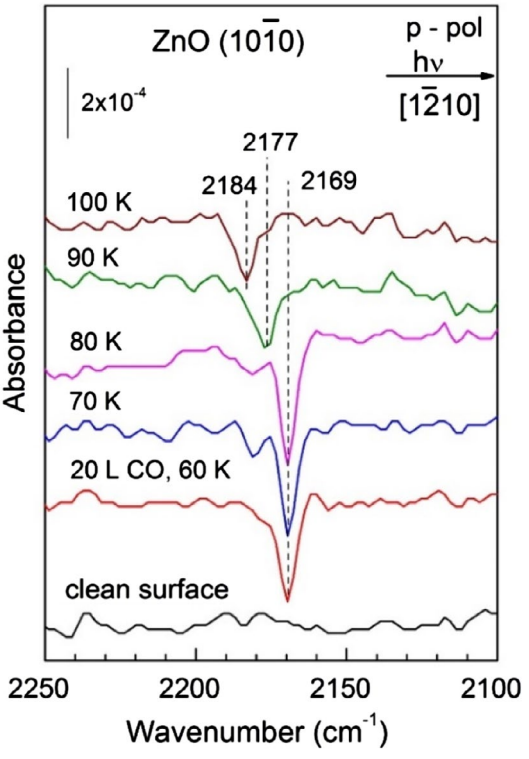

Figure 9. IRRA spectra obtained after exposing ZnO(1 0 $\bar{1}$ 0) to CO at 60 K and subsequently heating to the indicated temperatures [48]. The spectra were measured with p-polarized light along the [1 $\bar{2}$ 1 0] azimuth. Source: Copyright © 2016 Elsevier.

We then elevated the sample temperature to further examine the thermal stability of the adsorbed CO species and the influence of coverage on the CO vibrational frequency. Upon heating to 80 K, the CO band remains unchanged both in intensity and frequency, indicating that the full CO monolayer is stable on ZnO(1 0 $\bar{1}$ 0) up to 80 K. This observation is in good agreement with the binding energy of CO adsorbates as deduced from earlier experimental work (0.22 eV) [102] and density functional theory (DFT) calculations (0.24 eV) [103] for a saturated CO monolayer on this mixed-terminated surface.

When further increasing the sample temperature, the CO band was observed to shift to 2177 cm^{-1} at 90 K and then to 2184 cm^{-1} at 100 K. Simultaneously, the CO band decreased in intensity, which is explained by a partial desorption of CO molecules. It should be noted that CO adsorption on ZnO(1 0 $\bar{1}$ 0) at 100 K leads to a maximum coverage of 0.5 ML only, with a binding energy of 0.32–0.36 eV as deduced from experiments [102,104] and DFT calculations [103].

In order to identify the adsorption geometry of CO on the ZnO(1 0 $\bar{1}$ 0) surface, additional IR experiments have been performed with p-polarized light incident along the [0 0 0 1] direction at 70 K (not shown), and similar results were obtained [48]. The present results clearly demonstrate an absence of azimuthal dependence,

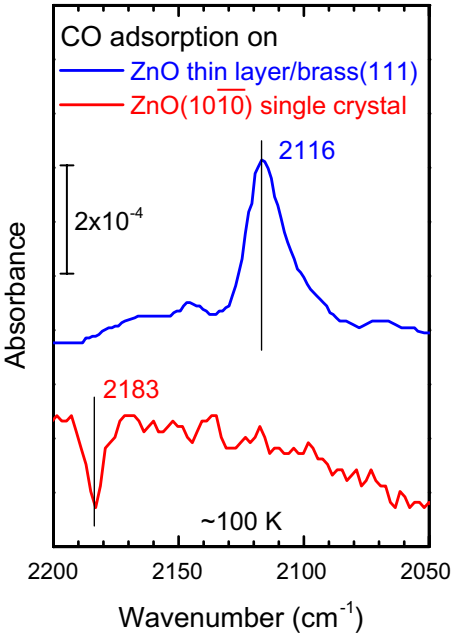

Figure 10. Comparison of IRRA spectra for the adsorption of CO on ZnO thin layer/brass(1 1 1) [105] and ZnO(1 0 $\bar{1}$ 0) substrate [48] at recorded for a substrate temperature of 100 K.

suggesting that the adsorbed CO molecules exhibit a mainly upright orientation. This is in line with a slightly tilted geometry of CO on ZnO(1 0 $\bar{1}$ 0), where the IR signals with $p_{t,x}$ (the tangential component of electric filed vector of p-polarized light) and s-polarized light are too weak to be detected.

In order to demonstrate the difference between IRRAS data recorded for single-crystal oxides and oxide thin films supported on a metal, in Figure 10 we show the comparison of IRRAS data recorded for CO adsorbed on a thin ZnO adlayer (~2 ML) grown on a brass(1 1 1) substrate [105] and for CO adsorbed on a mm-thick ZnO(1 0 $\bar{1}$ 0) substrate [48]. The total measurement times were the same (4 min). Clearly, the signs of the vibrational bands are opposite (see the discussion in the Introduction). While the relative change in absorbance caused by excitation of the CO stretching vibration is of comparable size (~2×10^{-4}) for both surfaces, the signal-to-noise (*S*/*N*) ratio in the spectrum recorded for CO adsorbed on the ZnO thin layer supported by a metal sample is much better than that for the ZnO(1 0 $\bar{1}$ 0) substrate. This can be understood by considering that, for the thin layer, the supporting metal substrate acts as a mirror and increases the total intensity of the reflected IR-light to a value which is comparable to that for metal substrates. For the thick ZnO substrate, on the other hand, the reflectivity is much lower (a refractive index of 1.9 corresponds to a reflectivity of 14.2% for p-polarized light at 80°) [22]. This reduction in reflectivity (roughly by a factor of 7) requires longer measurement times. To get the same *S*/*N* ratio than for metals, an increase of 7^2 i.e. ~50 is required. Also, for other dielectrics, reflectivity and,

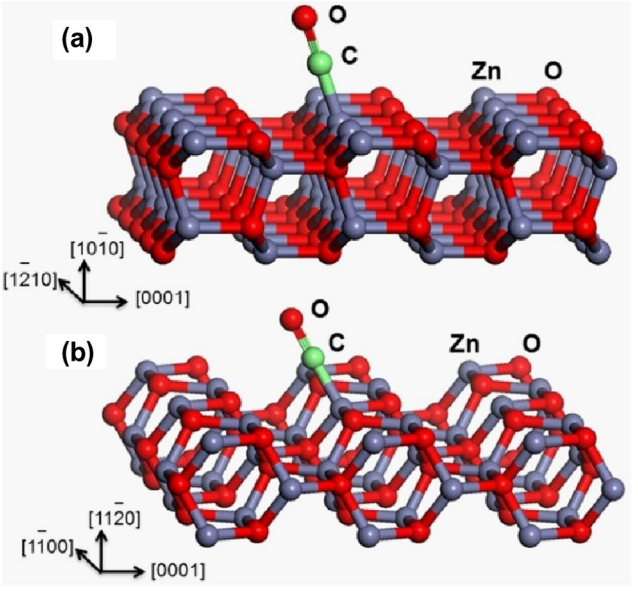

Figure 11. Ball-and-stick model for the adsorption of CO mixed-terminated ZnO surfaces: (a) ZnO(1 0 $\bar{1}$ 0); (b) ZnO(1 1 $\bar{2}$ 0)[48]. Color: oxygen (CO) – red, carbon – green, oxygen (ZnO) – red, zinc – gray. Source: Copyright © 2016 Elsevier.

correspondingly, sensitivity are low, increasing measurement times for IRRAS on bulk oxides and dielectrics by one to two orders of magnitude relative to metals.

4.2. CO/ZnO(1 1 $\bar{2}$ 0) [48]

Aside from(1 0 $\bar{1}$ 0), the mixed-terminated (1 1 $\bar{2}$ 0)surface is another nonpolar surface of ZnO, which exposes coordinatively unsaturated ZnO dimers (Figure 11(b)). The surface energy of ZnO(1 1 $\bar{2}$ 0)is found by the DFT calculations to be only slightly higher than that of ZnO(1 0 $\bar{1}$ 0), but much lower than those of the O- and Zn-terminated polar surfaces [106]. Figure 12(a) shows the IRRA spectra recorded with p-polarized light incident along the [0 0 0 1] direction after exposing the clean ZnO(1 1 $\bar{2}$ 0)surface to CO at 110 K. At low coverage (0.2 L CO), a single CO stretching vibrational band at 2190 cm^{-1} was observed. With increasing doses of CO at 110 K, this band shifts gradually to lower frequencies and eventually reaches 2181 cm^{-1} at saturation coverage, accompanied by a substantial increase in intensity.

The coverage-dependent frequency shift was also observed when reducing the CO coverage as a result of thermal desorption. After saturation coverage of CO on ZnO, (1 1 $\bar{2}$ 0)was achieved by exposing to CO gas at a substrate temperature of 110 K, the sample was subsequently heated to higher temperatures. The corresponding spectra are displayed in Figure 12(b). At 120 K, the CO molecules desorb partially, as confirmed by the intensity decrease in the CO band. At the same

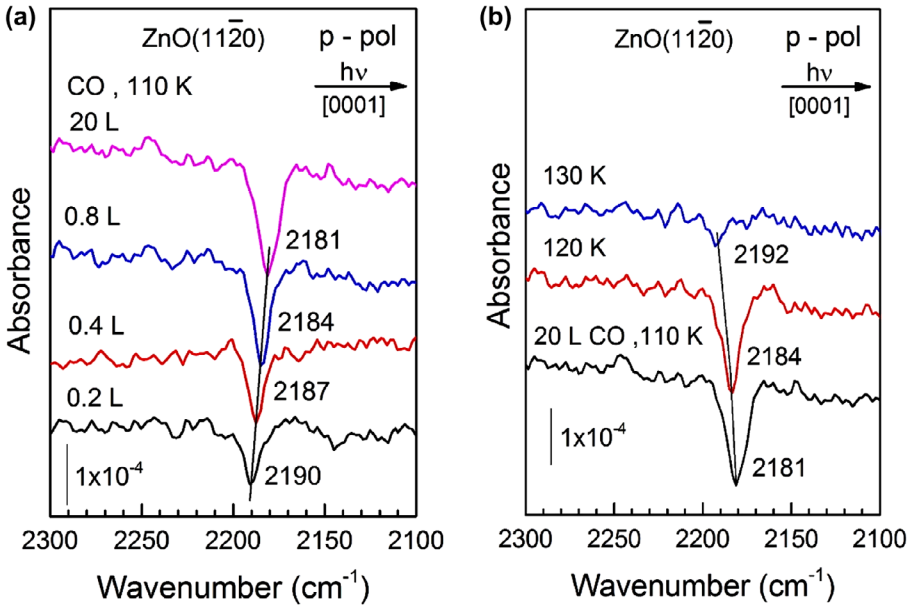

Figure 12. IRRA spectra obtained after (a) exposing ZnO(1 1 $\bar{2}$ 0) to different doses of CO at 110 K and (b) subsequently heating to indicated temperatures [48]. The spectra were measured with p-polarized light along the [0 0 0 1] azimuth. Source: Copyright © 2016 Elsevier.

time, the frequency also shifted slightly from 2181 to 2184 cm^{-1}. When increasing the surface temperature up to 130 K, CO molecules almost completely desorbed from the surface, in very good agreement with the TDS results reported for CO adsorbed on ZnO(1 0 $\bar{1}$ 0) [104]. This observation indicates that CO molecules interact with the two nonpolar ZnO(1 1 $\bar{2}$ 0)and ZnO(1 0 $\bar{1}$ 0) surfaces in a similar fashion. Importantly, at 130 K, a weak but unambiguous feature was resolved at 2192 cm^{-1}, which is attributed to isolated CO species (singletons). The frequency of this feature is in excellent agreement with the CO-bands reported for ZnO nanoparticles (2190–2192 cm^{-1}) [100,101,107].

Given the similar nature of CO interaction with the ZnO(1 0 $\bar{1}$ 0) surfaces, CO adsorption on ZnO(1 1 $\bar{2}$ 0)at 110 K probably also leads to a maximum coverage about 0.5 ML. In order to investigate the CO adsorption at a full monolayer, we have carried out additional experiments at lower temperatures. As shown in Figure 13, after exposing the clean ZnO(1 1 $\bar{2}$ 0)surface to 1 L CO at 70 K, only a single ν(C–O) band was detected at 2170 cm^{-1}. This peak remains constant, both in frequency and intensity, upon heating to 80 K. These results are very similar to those obtained for the ZnO(1 0 $\bar{1}$ 0) surface (see Figure 9), indicating that a full monolayer coverage is achieved for CO adsorption on ZnO(1 1 $\bar{2}$ 0)at 70 K.

Overall, for CO adsorption on ZnO(1 1 $\bar{2}$ 0)only one negative CO vibrational band was detected for p-polarized light, while no signal was observed for the s-polarized light. This indicates that the dynamic dipole moment of the CO stretching vibration mainly interacts with the $p_{n,z}$ component (the normal component of

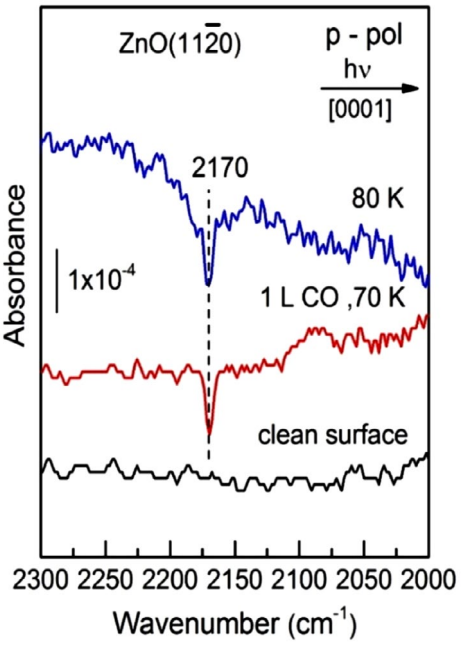

Figure 13. IRRAS data obtained after exposing ZnO(1 1 $\bar{2}$ 0)to CO at 70 K and subsequently heating to 80 K [48]. The spectra were measured with p-polarized light along the [0 0 0 1] axis. Source: Copyright © 2016 Elsevier.

electric field vector of p-polarized light). CO is bound to the surface Zn^{2+} sites of ZnO(1 1 $\bar{2}$ 0) with a configuration as shown schematically in Figure 11. Though a tilted geometry (41.4° to the surface normal) has been proposed for CO on ZnO(1 1 $\bar{2}$ 0)[102], we thus have to conclude based on our experimental observations that, when using s-polarized light, the signal is so weak that it cannot be detected, as discussed for ZnO(1 0 $\bar{1}$ 0).

The coverage-induced frequency shift is attributed to the lateral adsorbate-adsorbate interactions, including both dynamic and substrate-mediated static interactions [108,109]. For CO/oxide systems, the two effects lead to opposite frequency shifts. The dynamic interaction originates from the dipole-dipole coupling between adsorbed CO molecules and results in a blue-shift in frequency (as observed for CO/metal systems [110]). The coupling occurs when adjacent oscillators show the same intrinsic frequency and are oriented parallel to each other. The static shift originates from the interaction between CO adsorbates through the substrate and depends on the ability of the adsorbed molecules to transmit negative charge to the neighboring adsorption sites [111]. The substrate-mediated static interaction leads to red-shift in frequency when the coverage is increased.

The frequency shift of the ν(C–O) band comes as the result of the sum of the above two adsorbate-adsorbate interactions: $\Delta\nu = \Delta\nu_{dyn} + \Delta\nu_{stat}$. Whereas image dipoles provide an important contribution [112,113] in case of CO bounds to

metal substrates, they are absent for CO adsorption on dielectric (oxide) substrates. In this case, the dynamic effect originates from the direct (through-space) dipole-dipole coupling between adsorbed CO molecules. The contribution of the dynamic adsorbate-adsorbate interaction ($\Delta\nu_{dyn} = \nu - \nu_0$) can be estimated by the modified Hammaker equation [114]:

$$\nu = \nu_0\left(1 + \frac{\alpha_\upsilon\theta\Sigma_0}{1 + \alpha_e\theta\Sigma_0}\right)^{\frac{1}{2}}$$

where ν_0 is the frequency of isolated CO (singleton), α_ν the dynamic polarizability, Σ_0 the direct dipole sum, and α_e the electronic polarizability. As shown in Figure 13, the ν_0 of isolated CO adsorbed on ZnO(1 1 $\bar{2}$ 0)was observed at 2192 cm^{-1}. Based on the α_ν (0.057 Å^3) and α_e (1.89 Å^3) values given in the literature [112], the $\Delta\nu_{dyn}$ can be estimated to be +3.6 cm^{-1} at 0.5 ML and +6.5 cm^{-1} at full monolayer. At θ = 1 ML, the CO band was observed at 2170 cm^{-1} for ZnO(1 1 $\bar{2}$ 0) with a total frequency shift $\Delta\nu$ = −22 cm^{-1} compared to the ν_0 = 2192 cm^{-1} for isolated CO (Figure 12(b)). Correspondingly, the contribution of the static shift ($\Delta\nu_{stat}$) is deduced to be −28.5 cm^{-1}. For the ZnO(1 0 $\bar{1}$ 0) surface, the $\Delta\nu$ value is estimated to be −23 cm^{-1} (ν_0 = 2192 cm^{-1}, ν = 2169 cm^{-1} at θ = 1 ML), and $\Delta\nu_{stat}$ = −29.5 cm^{-1}. These results indicate that the coverage-induced frequency shift for CO adsorption on ZnO surfaces originates predominantly from the substrate-mediated static interaction in CO adlayers, whereas the contribution of the dynamic effect is relatively small.

Finally, a closer analysis of the present IR data reveals that the CO bands become broader and asymmetric at intermediate coverages on both ZnO(1 0 $\bar{1}$ 0) and ZnO(1 1 $\bar{2}$ 0)surfaces. This could be related to the presence of different variants of the CO nearest neighbors at moderate coverages, which correspond to lateral interaction effects of different magnitude, thus leading to the appearance of several discrete bands as observed for ZnO powder samples [101,115].

4.3. CO_2/ZnO(1 0 $\bar{1}$ 0) [43]

IRRA spectra were recorded with both s- and p-polarized IR light incident along the [0 0 0 1] and [1 $\bar{2}$ 1 0] azimuthal directions after exposing the ZnO(1 0 $\bar{1}$ 0) sample to 1.5 Langmuir (L) of CO_2 at 100 K. A complete set of IRRAS data is shown in Figure 14 together with the powder data reproduced from the work of Noei et al. [116]. In the spectrum recorded with p-polarized light incident along the [0 0 0 1] azimuth, one positive band at 1591 cm^{-1} and one negative band at 1344 cm^{-1} are visible. The corresponding spectrum recorded with s-polarized light incident along the same direction does not exhibit any clear feature. For the [1 $\bar{2}$ 1 0] azimuth, however, we obtained rather different results (cf. Figure 14(b)). Here, distinct negative bands at 1340 cm^{-1} in the p-polarized spectrum and at 1584 cm^{-1} in the s-polarized spectrum were observed (Figure 14(b)).

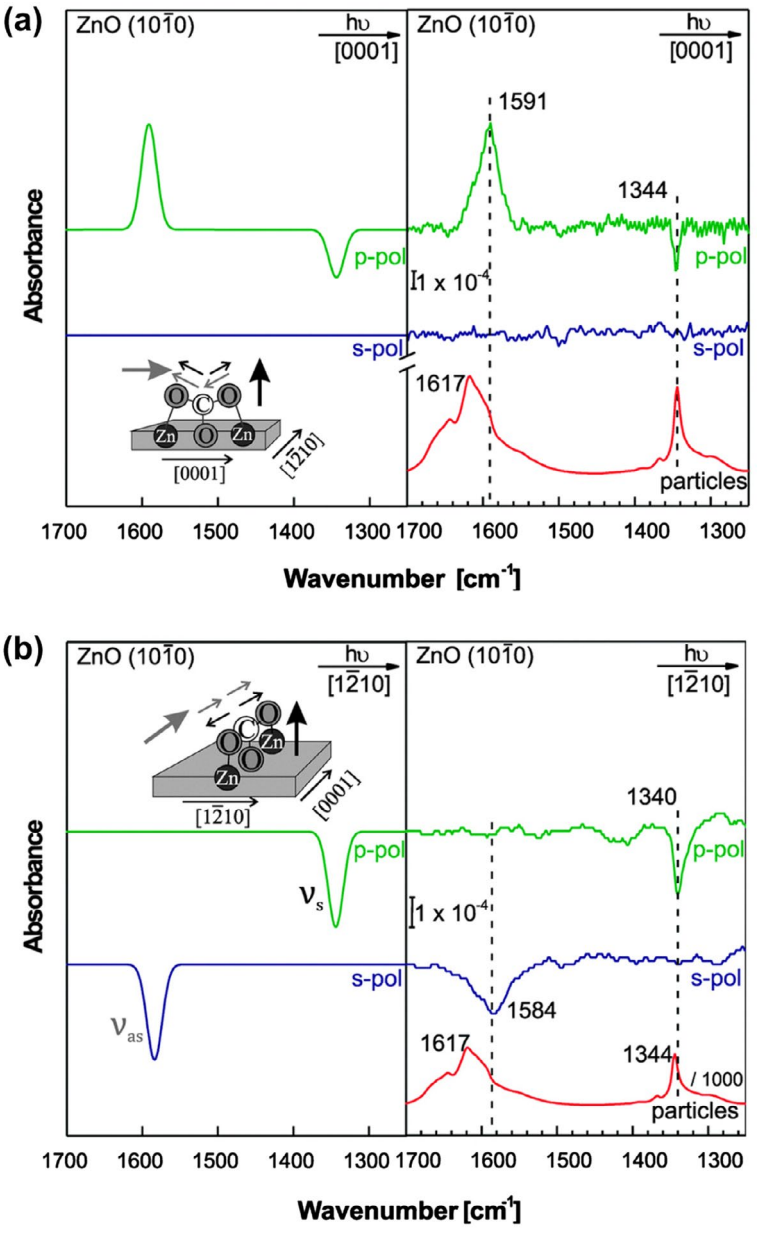

Figure 14. Expected signals in IRRA spectra based on calculations (left panel) and experimental IRRA spectra of CO_2 on ZnO(1 0 $\bar{1}$ 0) at a grazing incidence angle of 80° with s- and p-polarized light at 100 K (right panel) [43]. The sketch shows the orientation of the tridentate carbonate species on the surface with the arrows indicating the movement during the vibrations. The big light and dark gray arrows indicate the orientation of the TDM of the vibrations. Together with the experimental data recorded for the ZnO(1 0 $\bar{1}$ 0) single crystal, we show ZnO powder particle spectra [116]. (a) Incident beam along [0 0 0 1] and (b) [1 $\bar{2}$ 1 0] azimuth. Source: Copyright © 2014 The Royal Society.

The interpretation of the experimental IR data obtained for the carbonate species formed by exposing ZnO(1 0 $\bar{1}$ 0) substrates to CO_2 is challenging; the four spectra recorded for different polarizations and directions of incident light are all different. In order to assist the assignment of the different features, we will first predict the signs and intensities of the various IR bands by applying the set of rules described below (see Figure 20 for a sketch describing the decomposition of the incident IR light into the s- and p-polarized components).

(1) s-polarized light (electric field vector E_s parallel to the surface)
   (a) Only adsorbate vibrations with a TDM component orientated parallel to the surface and E_s are visible.
   (b) The sign of peaks in the IRRAS data is always negative.
(2) p-polarized light
   (a) A proper analysis requires the decomposition of the incident electric field vector into a tangential component, $E_{p,t}$, and a normal component, $E_{p,n}$.
   (b) The peaks related to the two different components $E_{p,t}$ and $E_{p,n}$ always have opposite sign.

(IRRAS data are typically recorded at an incidence angle that is greater than the Brewster angle. Under these conditions, in p-polarization, the sign of the band related to the *E*-vector in-plane component ($E_{p,t}$) is positive, whereas that resulting from the normal component ($E_{p,n}$) is negative.)

We now apply these rules to the adsorbate geometry of the carbonate species on this substrate proposed by Kotsis et al. on the basis of an extensive theoretical study [117]. This activated CO_2 adsorbate exhibits an upright geometry. The orientation of the molecular O–C–O-plane is orthogonal to the substrate and parallel to the [0 0 0 1] direction. For this geometry, the rules provided above allow to make the following predictions for the intensities and signs of the two most important carbonate vibrational bands. For the symmetric stretching vibration ν_s, the corresponding TDM, TDM_s, is orientated perpendicular to the surface, and thus no contribution should be observed in either azimuth for s-polarized light. For the asymmetric stretching vibrations ν_{as}, the corresponding TDM, TDM_{as}, is oriented parallel to the surface and points along the [0 0 0 1] azimuth. As a result, we predict a high intensity for s-polarized light incident along the [1 $\bar{2}$ 1 0]azimuth. After rotation of the sample by 90°, for light incident along the [0 0 0 1] azimuth, no signal should be seen. In the case of p-polarized light, the symmetric vibration ν_s should be visible with light incident along both high-symmetry directions, since in both cases, the normal component of the *E*-vector, $E_{p,n}$, can couple to the TDM of this vibration. Also from the asymmetric vibration ν_{as} a signal is expected, since in this case, the TDM is orientated parallel to the substrate, and can thus couple to the tangential component $E_{p,t}$ of p-polarized light, in case the direction of the

incident light is along the [0 0 0 1] azimuth. No excitation should occur when the p-polarized light is incident along the other high-symmetry azimuth, [1 $\bar{2}$ 1 0].

For a more quantitative analysis of the sign and intensity of the IRRAS bands, one has to calculate the reflectivity, e.g. using the three-phase model as described by Hansen et al. [23,118] and Mielezarski and Yoon [119] for dielectric materials. Within this approach, the reflectivity difference ΔR_i is calculated separately for each component i of the incident light (E_s, $E_{p,t}$, and $E_{p,n}$), by subtracting the reflectivity of the adsorbate-covered substrate (R_i) from that of the clean substrate (R_i^0) according to the following formula:

$$\Delta R_i(\theta) = R_i^0(\theta) - R_i(\theta)$$
$$R_i(\theta) = R_i^0(\theta)/10^{\Delta A i(\theta)}$$

where

$$R_s^0(\theta) = (|[\xi_3(\theta) - \xi_1(\theta)]/[\xi_3(\theta) + \xi_1(\theta)]|)^2$$

and

$$R_{pt}^0(\theta) = R_{pn}^0(\theta) = \left\{ \left[\frac{\xi_3(\theta)}{(n_3)^2} - \frac{\xi_1(\theta)}{(n_1)^2} \right] \Big/ \left[\frac{\xi_3(\theta)}{(n_3)^2} + \frac{\xi_1(\theta)}{(n_1)^2} \right] \right\}^2$$

with the absorbance ΔA_i

$$\Delta A_s(\theta) = -\frac{16\pi}{\ln 10} \left[\frac{\cos\theta}{n_3^2 - 1} \right] \frac{n_2 k_2 d_2}{\lambda}$$

$$\Delta A_{pt}(\theta) = -\frac{16\pi}{\ln 10} \left[\frac{\cos\theta}{\frac{\xi_3^2(\theta)}{n_3^4} - \cos^2\theta} \right] \left[-\frac{\xi_3^2(\theta)}{n_3^4} \right] \frac{n_2 k_2 d_2}{\lambda}$$

$$\Delta A_{pn}(\theta) = -\frac{16\pi}{\ln 10} \left[\frac{\cos\theta}{\frac{\xi_3^2(\theta)}{n_3^4} - cos^2\theta} \right] \frac{\sin^2\theta}{(n_2^2 + k_2^2)^2} \frac{n_2 k_2 d_2}{\lambda}$$

and

$$\xi_j(\theta) = \sqrt{\hat{n}_j^2 - n_1 \sin^2\theta}$$

$$\hat{n}_j = n_j + ik_j$$

where n_j is the refractive index of layer j, $\hat{n}$ denotes the complex index of refraction $n + ik$, k is the extinction coefficient, and d_2 refers to the thickness of the adsorbate layer.

Expected signals in IRRAS data based on calculations are displayed in Figure 14, left panels. When comparing to the experimental data, it has to be kept in mind that this simulation is based on a rather simple model. A number of additional effects is neglected. For example, contributions arising as a result from the thermal occupation of low-energy vibrations, e.g. frustrated rotations and translations, were not considered. The occupation of frustrated rotations results in dynamic tilt angles [120–122], which can make a vibration with a TDM orientated exclusively perpendicular to the surface also visible with s-polarized light. A detailed analysis of the IRRAS data considering the particular optical properties of dielectric surfaces in the context of the simple model described above yields a good agreement of the experimentally observed IR band magnitudes and signs with the theoretical predications assuming a carboxylate species with its backbone plane oriented parallel to the [0 0 0 1] azimuth and perpendicular to the surface.

4.4. IR signatures of photo-generated charge carriers in ZnO

In using a similar approach as reported in Section 3.4 for TiO_2, also in case of ZnO, the IR signature of photo-generated charge carriers was studied. In Figure 15 we show a series of spectra recorded after illumination of the substrates with

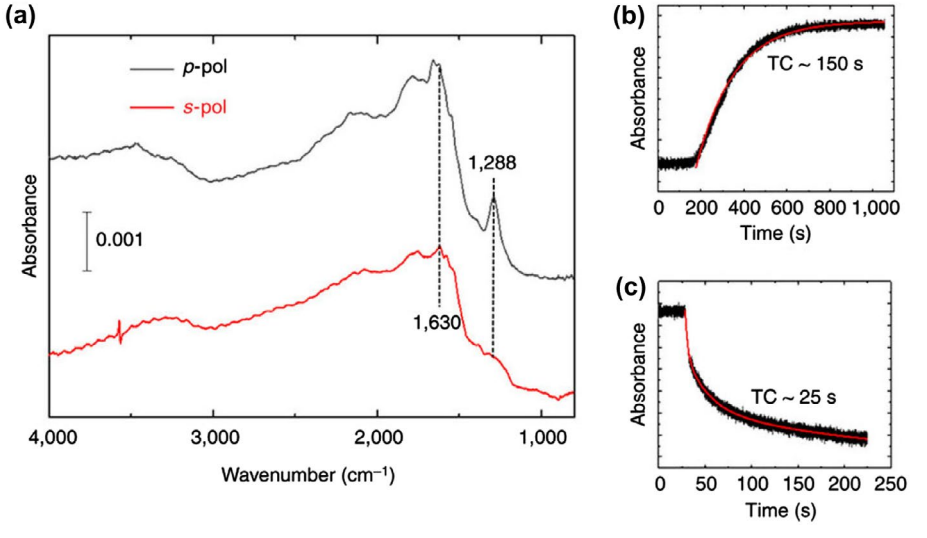

Figure 15. Steady state (during ultraviolet light irradiation) IR spectra (p- and s-polarization) of ZnO($1\,0\,\bar{1}\,0$) recorded at 118 K (a). Time dependence of the intensity of the sharp feature at 1630 cm^{-1} on starting (b) and terminating (c) ultraviolet irradiation at 75 K with the time constants (TC) indicated for the rise and decay of the signal [125]. Source: Copyright © 2015 Nature Publishing Group.

photons of 3.40 eV, an energy slightly larger than the band-gap of ZnO (3.3 eV). Clearly, also in this case, a sharp feature is seen in the IRRAS data. For ZnO, the main UV-induced absorption band is located at 1288 cm^{-1} and is accompanied by an absorption-edge-like feature at 1630 cm^{-1}. Using the so-called rapid scan method [123,124], the temporal evolution of these species could be determined and allowed to obtain an effective activation energy of −246 meV. In this case, a rather detailed theoretical analysis was carried out which provided strong evidence that the observation seen in the experimental data is in fact due to the excitation of hole polarons of intermediate coupling strength [125]. According to the theoretical analysis, these polarons are particular in the sense that they correspond to an intermediate size with a diameter of about 15 Å. Interestingly, the rather detailed analysis of the data allowed concluding that from the difference of the spectra seen for p- and s-polarized light the feature at 1288 cm^{-1} can actually be ascribed to a surface polaron. As in case of the TiO_2, these time-resolved (on a second time scale) data show the huge potential of IR spectroscopy to determine photophysical properties of oxide surfaces.

5. CeO_2

Ceria (CeO_2) has become a ubiquitous constituent in catalytic systems for a variety of applications over the last forty years [126,127]. The high catalytic activity, in particular for redox reactions, is connected with the facile reducibility of this oxide and the concomitant ability to supply lattice oxygen for a reaction. In an equally facile manner, the O vacancies are healed again in an oxygen-rich ambience, making ceria the ideal buffer system for oxygen in a catalytic process [128]. Ceria has three stable low-index crystallographic surfaces, (1 1 1), (1 1 0) and (1 0 0), which expose cerium cations and oxygen anions with different coordination environments. The ability to adsorb or give up oxygen varies between the different crystallographic surface orientations, and the corresponding redox-type reactions are likely to be different. Additionally, the chemistry of the same adsorbate proceeding on a fully oxidized CeO_2 surfaces may be substantially distinct from that on a reduced ceria surface due to different oxidation states of surface cerium cations [129]. Here, we present IRRAS results of CO adsorption on macroscopic monocrystalline ceria (1 1 1) and (1 1 0) surfaces.

5.1. CO/CeO_2(1 1 1) [42]

In the work by Yang et al., first the stretching frequency of CO adsorbed on a fully-oxidized, single crystalline CeO_2(1 1 1) surface ('stoichiometric surface') was determined using polarization-dependent IRRAS with the light incident along the [$\bar{1}$ 1 0] azimuth. The corresponding p-polarized data shown in Figure 16(a) reveal a single, sharp band at 2154 cm^{-1}, which can be assigned in a straightforward fashion to CO molecules bound to Ce^{4+} cations embedded in a perfect

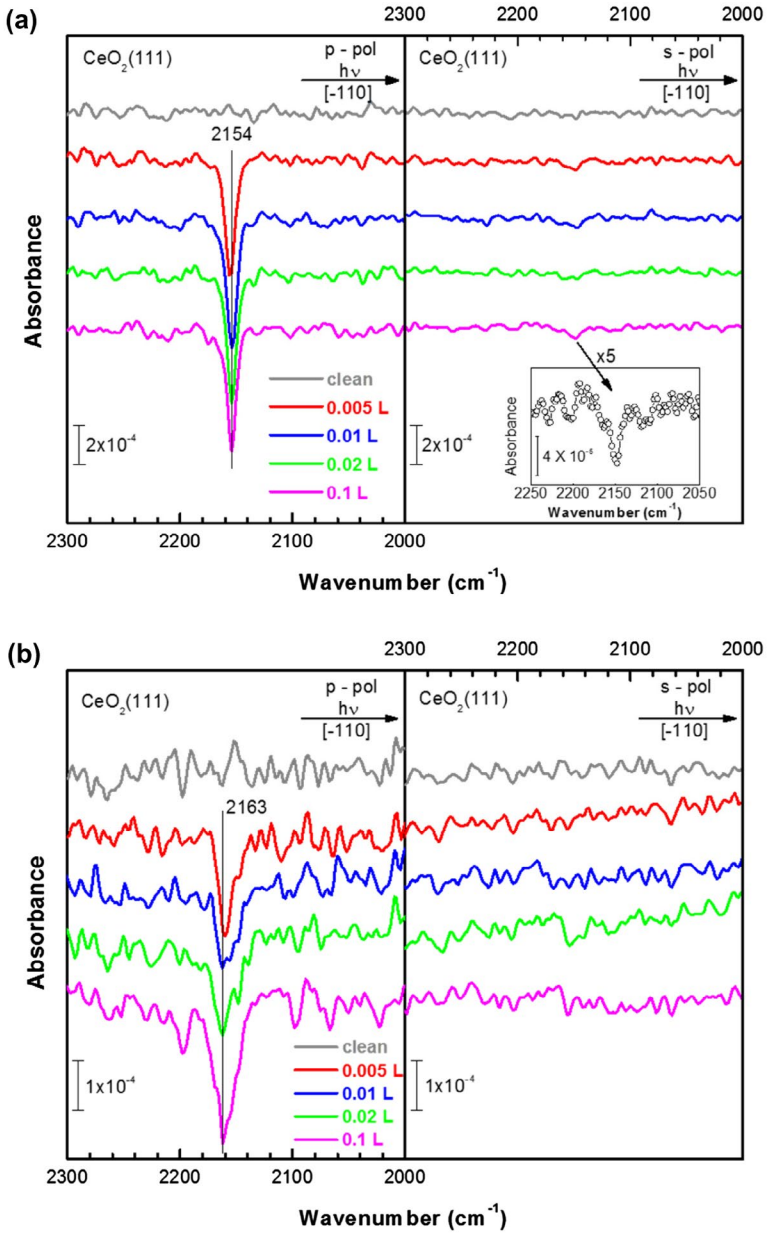

Figure 16. Experimental IRRA spectra of different doses of CO at around 70 K on oxidized (a) and reduced (b) CeO_2(1 1 1) at a grazing incidence angle of 80° with (left) p- and (right) s-polarized light incident along $[\bar{1}\,1\,0]$ [42]. Source: Copyright © 2014 The Royal Society.

monocrystalline surface environment (site 3 in Figure 17). The CO peak is negative, in accord with IR-data recorded for CO adsorbed on TiO_2 [40] and ZnO [48] surfaces. Only a very weak, also negative, feature was observed for s-polarized light. Almost identical results were obtained for the IR-light incident along the $[\bar{2}\,1\,1]$ azimuthal direction [42].

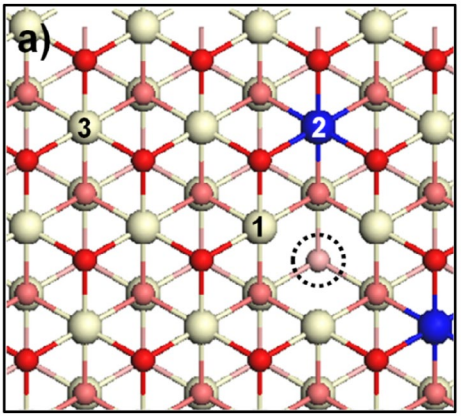

Figure 17. Ball-and-stick model of the CeO_2(1 1 1) surface (top view) with top-surface oxygen vacancy [42]. The position of the vacancy is indicated by the dashed circle. Color: red – top surface oxygen, light red – subsurface oxygen, white – Ce^{4+}, blue – Ce^{3+}. Source: Copyright © 2014 The Royal Society.

In a next step, oxygen vacancies were deliberately introduced on the CeO_2(1 1 1) surface by Ar^+ sputtering and annealing under UHV conditions ('reduced surface'). As deduced from XPS data, the oxygen vacancy density in the near-surface area of this sample amounts to approximately 9%. The corresponding IRRAS data shown in Figure 16(b) revealed a substantial broadening of the CO stretching peak, which is centered at around 2163 cm^{-1}. By applying a fitting procedure, which assumes the presence of only a single additional species (in addition to that observed at 2154 cm^{-1} for the clean surface), the deconvoluted data [42] clearly reveal the presence of a new species at 2163 cm^{-1}. This reduction-induced feature exhibits a blue-shift of roughly 10 cm^{-1} with respect to CO adsorbed on the stoichiometric CeO_2(1 1 1) surface. At the same time, the analysis of temperature-dependent IRRAS data revealed a slightly larger binding energy of CO on the reduced surface relative to the fully oxidized surface, 0.31 eV vs. 0.27 eV [42].

Such a small blue-shift in the stretching frequency of the CO bound to the defect-induced surface is unusual. On other oxides like TiO_2 the increased binding energy at defect sites (which is also observed for CO on CeO_2(1 1 1)) is accompanied by a red-shift in frequency [40]. In order to better understand the origins of this unexpected behavior and to assign the defect-induced band, Gong and co-workers have carried out first-principle DFT calculations [42]. The results of the calculations allowed to assign the defect-induced vibrational mode (2163 cm^{-1}) to CO adsorbed at 6-fold coordinated Ce^{4+} ions in the direct vicinity of the vacancy (site 1 in Figure 17). The interaction of CO with CeO_2 is very complex which was not discussed in [42]. The small blue-shift originates probably from a slight increase in the Lewis acidity of Ce^{4+} ions at the oxygen vacancies than that for the perfect sites. In this case the adsorbed CO molecules donate more electrons from the 5σ orbital to the defective Ce cations. The electron transfer from CO

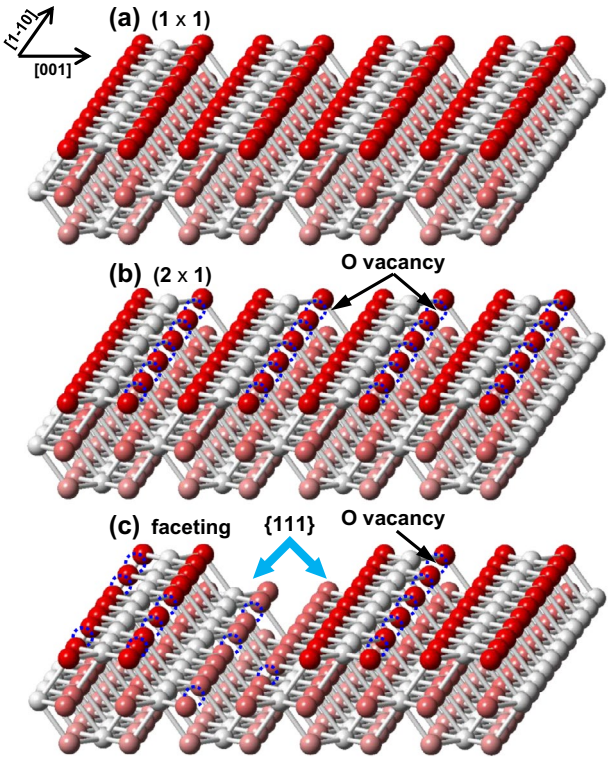

Figure 18. Structure evolution during reduction of the CeO_2(1 1 0) surface [50]. (a) The stoichiometric, fully oxidized (1 × 1) phase. (b) (2 × 1) reconstruction. (c) {1 1 1} nanofaceting. The oxygen vacancies are indicated by the dashed circles.

to the substrate strengthens the C–O bond, and thus leads to a blue-shift of the C–O stretching vibration.

5.2. CO/CeO_2(1 1 0) [50]

The stoichiometric, ideal bulk truncated (1 × 1) structure of the CeO_2(1 1 0) surface (Figure 18(a)) consists of two O rows sandwiching a row of Ce, all rows running along the [1 $\bar{1}$ 0] direction and is characterized by a well-defined LEED diffraction pattern (Figure 19(b)). Figure 19(a) shows IRRAS data recorded for this stoichiometric CeO_2(1 1 0) surface after exposure to CO at 80 K. The p-polarized spectrum exhibits a predominant peak at 2170 cm^{-1}, which is assigned to CO bound to Ce^{4+} cations embedded in a perfect monocrystalline surface environment.

After reducing the surface by annealing at 800 K under UHV conditions, the well-defined (1 × 1) LEED pattern of the ideally terminated CeO_2(1 1 0) single crystal surface changes to a clear, equally well-defined (2 × 1) LEED pattern (Figure 19(b)), revealing a new surface atomic arrangement. A general consensus on the precise geometric structure of this reduced phase has not yet been

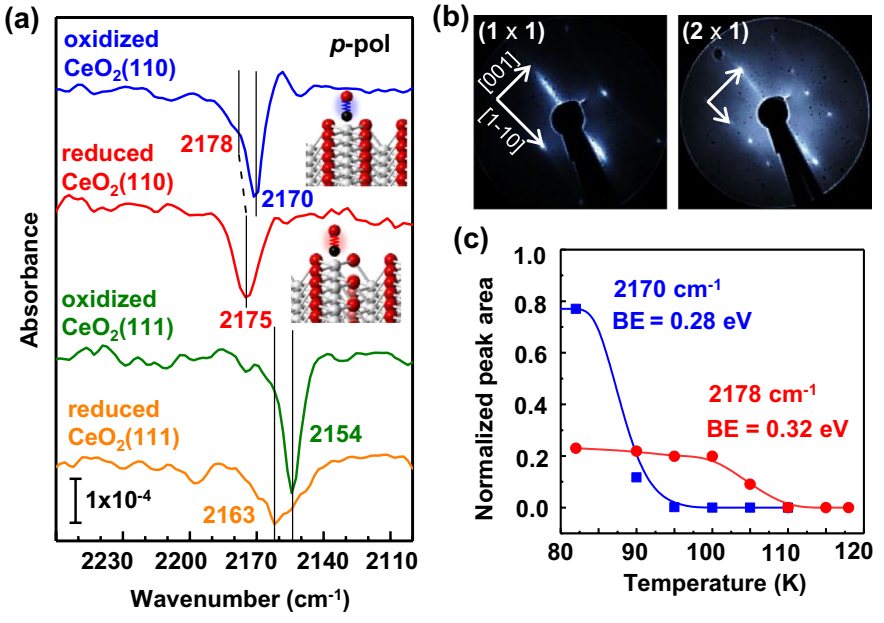

Figure 19. Surface structure of flat CeO_2(1 1 0). (a) IRRA spectra of 1 ML CO adsorption on oxidized (blue line) and reduced (red line) ceria (1 1 0) at 80 K with p-polarized light incident along the [1 $\bar{1}$ 0] azimuth. (b) LEED patterns of oxidized (left panel) and reduced (right panel) (1 1 0) surfaces. (c) Integrated intensity evolution of two spectral components of CO on oxidized (1 1 0) surface with increasing temperatures. For comparison, the IRRAS data of 1ML CO adsorption on oxidized and reduced CeO_2(1 1 1) [42] are shown in (a).

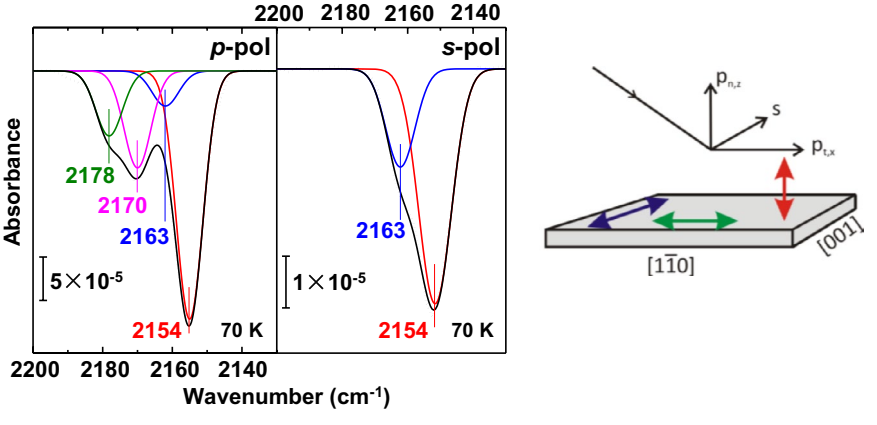

Figure 20. CeO_2(1 1 0) surface faceting probed by IRRAS after CO adsorption [50]. Fitting of p- and s-polarized spectra of faceted CeO_2(1 1 0) exposed to CO at 70 K with light incident along the [1 $\bar{1}$ 0] azimuth.

achieved. A tentative model based on the surface stoichiometry as deduced from the XPS-data is shown in Figure 18(b). According to this model, the CeO_2(1 1 0) surface is reconstructed, with 25% of the oxygen atoms missing. This structure

thus resembles a layer of Ce_2O_3. For this (2 × 1) reconstruction, adsorbed CO shows only one sharp CO band at 2175 cm^{-1} (Figure 19(a)), which is tentatively attributed to CO species adsorbed at Ce^{3+} ions. Unfortunately, accurate first-principle calculations which might aid such an assignment (as discussed in some of the previous examples) are not yet available for CO bound to this reconstructed surface. Note, that the Ce^{3+}-related CO band at 2178 cm^{-1} was also observed on the (1 × 1) surface as a minority species (Figure 19(a)). The temperature-dependent IRRAS data show that upon annealing the 2170 cm^{-1} band decreases quickly in intensity and disappears at 95 K, while the 2178 cm^{-1} band is found to disappear after heating to 110 K (Figure 19(c)). The corresponding binding energies obtained from an analysis of this temperature dependence amounted to 0.28 and 0.32 eV, respectively, indicating a stronger interaction between CO and the reduced Ce^{3+} sites.

Interestingly, subjecting the CeO_2(1 1 0) surface to repeated cycles of sputtering and annealing leads to further substantial changes, as evidenced by the IRRAS data displayed in Figure 20. At saturation coverage, the simultaneous observation of four CO bands in the p-polarized spectrum reveals unambiguously a severe restructuring of the reduced CeO_2(1 1 0) surface. The occurrence of these different bands was related to faceting, leading to {1 1 1} nanofacets separated by partially reduced (1 1 0) terrace. The band at 2170 cm^{-1} with an obvious shoulder at 2178 cm^{-1}, which is assigned to CO bound to perfect and defective sites on the (1 1 0) terrace, respectively. Two low-lying features emerge at 2154 and 2163 cm^{-1} which are characteristic for CO species adsorbed at oxidized and defective sites of {1 1 1} facets [42].

In order to identify the adsorption geometry of the various CO species bound to this strongly restructured surface, we have performed additional IRRAS experiments recorded with s-polarized light (Figure 20). S-polarized light is oriented parallel to the surface and perpendicular to the incidence plane. Only vibrational modes with a TDM orientated parallel to the surface can couple with this polarization, resulting in negative absorbance bands. In the s-polarized spectra (Figure 20), only two CO bands located at 2154 and 2163 cm^{-1} originating from CO adsorbed on (1 1 1) surfaces were detected. This observation is in perfect agreement with the fact that the {1 1 1} nanofacets are tilted with respect to the surface plane (see Figure 18(c)). As a result, CO molecules bound to this surface adopt an effectively tilted geometry with respect to the normal of the substrate, and therefore exhibit a weak signal also in the s-polarized spectra. In contrast, no CO bands assigned to (1 1 0) terraces were visible with s-polarized light, indicating that CO adsorbs to the (1 1 0) terrace in an upright orientation (see Figure 19(a)).

6. Summary

In this review, we have compiled the results of infrared spectroscopic studies of CO adsorption on three different oxide surfaces, TiO_2, ZnO and CeO_2. Using a newly

designed state-of-the-art UHV-IRRAS apparatus, we were able to conduct IRRAS measurements on macroscopic metal oxide single crystals in reflection geometry. These measurements demonstrate first that IRRAS applied to oxides has a huge potential and is not restricted to TiO_2, the material for which so far most IRRAS studies have been reported. Furthermore, these results demonstrate that CO is a very sensitive probe molecule to probe microscopic structural details of oxide surfaces, in particular the presence of surface oxygen vacancies. In many cases, the CO stretch frequencies are clearly different for different crystallographic surface orientations, and the frequencies are also sensitive to surface atomic rearrangements occurring upon e.g. reduction of the oxidic substrates. The IRRAS method has also been successfully applied to study of the photo-oxidation of CO over rutile- and anatase-TiO_2 surface and to investigate photophysical properties (e.g. the formation of photo-induced polarons) in the case of TiO_2 and ZnO substrates. With the assistance of a polarizer, the determination of adsorption geometry of molecular adsorbates on oxide substrates becomes possible, as demonstrated here for the case of CO_2 adsorbed on ZnO(1 0 $\bar{1}$ 0). We feel that the full potential of the UHV-IRRAS approach has not yet been exploited, in the future this technique should be applied to more oxides. We would also like to stress the enormous potential of IR spectroscopy for probing photophysical properties of oxide surfaces.

Disclosure statement

No potential conflict of interest was reported by the authors.

References

[1] S.D. Jackson and J.S. Hargreaves, *Metal Oxide Catalysis*, Wiley-VCH Verlag GmbH & Co. KGaA, Weinheim, 2009.
[2] G. Korotcenkov, Mater. Sci. Eng. B 139 (2007) p.1.
[3] P.V. Kamat, Chem. Rev. 93 (1993) p.267.
[4] X. Yu, T.J. Marks and A. Facchetti, Nat. Mater. 15 (2016) p.383.
[5] S. Rühle, A.Y. Anderson, H.-N. Barad, B. Kupfer, Y. Bouhadana, E. Rosh-Hodesh and A. Zaban, J. Phys. Chem. Lett. 3 (2012) p.3755.
[6] D. Ficai, O. Oprea, A. Ficai and A.M. Holban, Curr. Proteomics 11 (2014) p.139.
[7] S. Andreescu, M. Ornatska, J.S. Erlichman, A. Estevez and J.C. Leiter, *Biomedical applications of metal oxide nanoparticles*, in *Fine Particles in Medicine and Pharmacy*, E. Matijević, ed., Springer, Boston, MA, 2012, p.57–100.
[8] N. Eliaz, *Degradation of Implant Materials*, Springer, New York, 2012.
[9] G. Ertl and H.-J. Freund, Phys. Today 52 (1999) p.3.
[10] G. Ertl, Angew. Chem. Int. Ed. 47 (2008) p.3524.
[11] V.E. Henrich and P.A. Cox, *The Surface Science of Metal Oxides*, Cambridge University Press, Cambridge, 1994.
[12] M.A. Barteau, Chem. Rev. 96 (1996) p.1413.
[13] U. Diebold, Surf. Sci. Rep. 48 (2003) p.53.
[14] F.M. Hoffmann, Surf. Sci. Rep. 3 (1983) p.107.
[15] P. Hollins and J. Pritchard, Prog. Surf. Sci. 19 (1985) p.275.

[16] B.E. Hayden, *Reflection absorption infrared spectroscopy*, in *Vibrational Spectroscopy of Molecules on Surfaces*, J.T. Yates and T.E. Madey, eds., Springer, Boston, MA, 1987, p.267–344.
[17] R.P. Eischens and W.A. Pliskin, Adv. Catal. 10 (1958) p.1.
[18] R.G. Greenler, D.R. Snider, D. Witt and R.S. Sorbello, Surf. Sci. 118 (1982) p.415.
[19] S.A. Francis and A. Ellison, J. Opt. Soc. Am. 49 (1959) p.131.
[20] R.G. Greenler, J. Chem. Phys. 44 (1966) p.310.
[21] B.E. Hayden, A. King and M.A. Newton, J. Phys. Chem. B 103 (1999) p.203.
[22] J. Kattner and H. Hoffmann, *External reflection spectroscopy of thin films on dielectric substrates*, in *Handbook of Vibrational Spectroscopy*, J.M. Chalmers and P.R. Griffiths, eds., John Wiley & Sons, Chichester, 2002, p.1009–1027.
[23] W.N. Hansen, J. Opt. Soc. Am. 58 (1968) p.380.
[24] H. Kuhlenbeck, S. Shaikhutdinov and H.-J. Freund, Chem. Rev. 113 (2013) p.3986.
[25] H.-J. Freund and D.W. Goodman, *Ultrathin oxide films*, in *Handbook of Heterogeneous Catalysis*, 2nd ed., G. Ertl, H. Knözinger, F. Schüth and J. Weitkamp, eds., Wiley-VCH Verlag GmbH & Co. KGaA, Weinheim, 2008, p.1309–1338.
[26] G.H. Vurens, M. Salmeron and G.A. Somorjai, Prog. Surf. Sci. 32 (1989) p.333.
[27] H.-J. Freund and G. Pacchioni, Chem. Soc. Rev. 37 (2008) p.2224.
[28] G. Kresse, M. Schmid, E. Napetschnig, M. Shishkin, L. Köhler and P. Varga, Science 308 (2005) p.1440.
[29] H. Grönbeck, J. Phys. Chem. B 110 (2006) p.11977.
[30] M. Sterrer, T. Risse, U. Martinez Pozzoni, L. Giordano, M. Heyde, H.-P. Rust, G. Pacchioni and H.-J. Freund, Phys. Rev. Lett. 98 (2007) p.096107.
[31] H.-J. Freund, Surf. Sci. 601 (2007) p.1438.
[32] G. Pacchioni and H.-J. Freund, Chem. Rev. 113 (2013) p.4035.
[33] G. Pacchioni, Chem. Rec. 14 (2014) p.910.
[34] C.T. Campbell, Surf. Sci. Rep. 27 (1997) p.1.
[35] M. Schiek, K. Al-Shamery, M. Kunat, F. Traeger and C. Wöll, Phys. Chem. Chem. Phys. 8 (2006) p.1505.
[36] C. Rohmann, Y. Wang, M. Muhler, J. Metson, H. Idriss and C. Wöll, Chem. Phys. Lett. 460 (2008) p.10.
[37] Y. Wang, A. Glenz, M. Muhler and C. Wöll, Rev. Sci. Instrum. 80 (2009) p.113108.
[38] M. Xu, Y. Gao, Y. Wang and C. Wöll, Phys. Chem. Chem. Phys. 12 (2010) p.3649.
[39] M. Xu, Y. Gao, E.M. Moreno, M. Kunst, M. Muhler, Y. Wang, H. Idriss and C. Wöll, Phys. Rev. Lett. 106 (2011) p.138302.
[40] M. Xu, H. Noei, K. Fink, M. Muhler, Y. Wang and C. Wöll, Angew. Chem. Int. Ed. 51 (2012) p.4731.
[41] M. Xu, H. Noei, M. Buchholz, M. Muhler, C. Wöll and Y. Wang, Catal. Today 182 (2012) p.12.
[42] C. Yang, L.-L. Yin, F. Bebensee, M. Buchholz, H. Sezen, S. Heissler, J. Chen, A. Nefedov, H. Idriss, X.-Q. Gong and C. Wöll, Phys. Chem. Chem. Phys. 16 (2014) p.24165.
[43] M. Buchholz, P.G. Weidler, F. Bebensee, A. Nefedov and C. Wöll, Phys. Chem. Chem. Phys. 16 (2014) p.1672.
[44] M. Buchholz, Q. Li, H. Noei, A. Nefedov, Y. Wang, M. Muhler, K. Fink and C. Wöll, Top. Catal. 58 (2015) p.174.
[45] M. Buchholz, M. Xu, H. Noei, P. Weidler, A. Nefedov, K. Fink, Y. Wang and C. Wöll, Surf. Sci. 643 (2016) p.117.
[46] M. Setvin, M. Buchholz, W. Hou, C. Zhang, B. Stöger, J. Hulva, T. Simschitz, X. Shi, J. Pavelec, G.S. Parkinson, M. Xu, Y. Wang, M. Schmid, C. Wöll, A. Selloni and U. Diebold, J. Phys. Chem. C 119 (2015) p.21044.

[47] C. Yang, F. Bebensee, A. Nefedov, C. Wöll, T. Kropp, L. Komissarov, C. Penschke, R. Moerer, J. Paier and J. Sauer, J. Catal. 336 (2016) p.116.
[48] M. Buchholz, X. Yu, C. Yang, S. Heißler, A. Nefedov, Y. Wang and C. Wöll, Surf. Sci. 652 (2016) p.247.
[49] X. Yu, Z. Zhang, C. Yang, F. Bebensee, S. Heissler, A. Nefedov, M. Tang, Q. Ge, L. Chen, B.D. Kay, Z. Dohnálek, Y. Wang and C. Wöll, J. Phys. Chem. C 120 (2016) p.12626.
[50] C. Yang, X. Yu, S. Heißler, A. Nefedov, S. Colussi, J. Llorca, A. Trovarelli, Y. Wang and C. Wöll, Angew. Chem. Int. Ed. 56 (2017) p.375.
[51] N.G. Petrik and G.A. Kimmel, J. Phys. Chem. Lett. 3 (2012) p.3425.
[52] X. Lin, Y. Yoon, N.G. Petrik, Z. Li, Z.-T. Wang, V.-A. Glezakou, B.D. Kay, I. Lyubinetsky, G.A. Kimmel, R. Rousseau and Z. Dohnálek, J. Phys. Chem. C 116 (2012) p.26322.
[53] G.A. Kimmel, M. Baer, N.G. Petrik, J. VandeVondele, R. Rousseau and C.J. Mundy, J. Phys. Chem. Lett. 3 (2012) p.778.
[54] N.G. Petrik, M.A. Henderson and G.A. Kimmel, J. Phys. Chem. C 119 (2015) p.12262.
[55] N.G. Petrik, M.A. Henderson and G.A. Kimmel, J. Phys. Chem. C 119 (2015) p.12273.
[56] M. Xu, Y. Cao, R. Xu, S. Hu and S. Yan, Phys. Chem. Chem. Phys. 16 (2014) p.23711.
[57] M. Xu, Y. Wang, S. Hu, R. Xu, Y. Cao and S. Yan, Phys. Chem. Chem. Phys. 16 (2014) p.14682.
[58] Y. Cao, S. Hu, M. Yu, S. Yan and M. Xu, Phys. Chem. Chem. Phys. 17 (2015) p.23994.
[59] Y. Cao, S. Hu, M. Yu, T. Wang, S. Huang, S. Yan and M. Xu, Phys. Chem. Chem. Phys. 18 (2016) p.17660.
[60] A. Mattsson, S. Hu, K. Hermansson and L. Österlund, J. Vac. Sci. Technol. A 32 (2014) p.061402.
[61] A. Mattsson, S. Hu, K. Hermansson and L. Österlund, J. Chem. Phys. 140 (2014) p.034705.
[62] O. Gamba, H. Noei, J. Pavelec, R. Bliem, M. Schmid, U. Diebold, A. Stierle and G.S. Parkinson, J. Phys. Chem. C 119 (2015) p.20459.
[63] K.I. Hadjiivanov and G.N. Vayssilov, Adv. Catal. 47 (2002) p.307.
[64] C. Lamberti, A. Zecchina, E. Groppo and S. Bordiga, Chem. Soc. Rev. 39 (2010) p.4951.
[65] M. Buchholz, *UHV-FTIRS-Untersuchungen an einkristallinen Oxidoberflaechen* [UHV-FTIRS investigations on single-crystal oxide surfaces], KIT Scientific Publishing, Karlsruhe, 2014.
[66] A.L. Linsebigler, G. Lu and J.T. Yates, Chem. Rev. 95 (1995) p.735.
[67] A. Fujishima and K. Honda, Nature 238 (1972) p.37.
[68] T.L. Thompson and J.T. Yates, Chem. Rev. 106 (2006) p.4428.
[69] M. Grätzel, Nature 414 (2001) p.338.
[70] Y. Furubayashi, T. Hitosugi, Y. Yamamoto, K. Inaba, G. Kinoda, Y. Hirose, T. Shimada and T. Hasegawa, Appl. Phys. Lett. 86 (2005) p.252101.
[71] S. Moser, L. Moreschini, J. Jaćimović, O.S. Barišić, H. Berger, A. Magrez, Y.J. Chang, K.S. Kim, A. Bostwick, E. Rotenberg, L. Forró and M. Grioni, Phys. Rev. Lett. 110 (2013) p.196403.
[72] K. Szot, M. Rogala, W. Speier, Z. Klusek, A. Besmehn and R. Waser, Nanotechnology 22 (2011) p.254001.
[73] M. Kunat, F. Traeger, D. Silber, H. Qiu, Y. Wang, A.C. van Veen, C. Wöll, P.M. Kowalski, B. Meyer, C. Hättig and D. Marx, J. Chem. Phys. 130 (2009) p.144703.
[74] G. Pacchioni, G. Cogliandro and P.S. Bagus, Surf. Sci. 255 (1991) p.344.
[75] Y. Zhao, Z. Wang, X. Cui, T. Huang, B. Wang, Y. Luo, J. Yang and J. Hou, J. Am. Chem. Soc. 131 (2009) p.7958.
[76] A. Fujishima, X. Zhang and D.A. Tryk, Surf. Sci. Rep. 63 (2008) p.515.
[77] M.A. Henderson, Surf. Sci. Rep. 66 (2011) p.185.
[78] K. Kalyanasundaram and M. Grätzel, Coord. Chem. Rev. 177 (1998) p.347.

[79] I. Mehdaoui and T. Klüner, Phys. Rev. Lett. 98 (2007) p.037601.
[80] A. Linsebigler, G. Lu and J.T. Yates, J. Phys. Chem. 100 (1996) p.6631.
[81] M.A. Henderson, Surf. Sci. 400 (1998) p.203.
[82] A. Linsebigler, G. Lu and J.T. Yates, J. Chem. Phys. 103 (1995) p.9438.
[83] X. Wu, A. Selloni and S.K. Nayak, J. Chem. Phys. 120 (2004) p.4512.
[84] D. Pillay and G.S. Hwang, J. Chem. Phys. 125 (2006) p.144706.
[85] Y. Ji, B. Wang and Y. Luo, J. Phys. Chem. C 117 (2013) p.956.
[86] N.G. Petrik and G.A. Kimmel, J. Phys. Chem. Lett. 4 (2013) p.344.
[87] F. Labat, P. Baranek, C. Domain, C. Minot and C. Adamo, J. Chem. Phys. 126 (2007) p.154703.
[88] H. Sezen, M. Buchholz, A. Nefedov, C. Natzeck, S. Heissler, C. Di Valentin and C. Wöll, Sci. Rep. 4 (2014) p.3808.
[89] T. Berger and J.A. Anta, Anal. Chem. 84 (2012) p.3053.
[90] T. Berger, J.A. Anta and V. Morales-Flórez, J. Phys. Chem. C 116 (2012) p.11444.
[91] D.A. Panayotov, S.P. Burrows and J.R. Morris, J. Phys. Chem. C 116 (2012) p.4535.
[92] D.M. Savory, D.S. Warren and A.J. McQuillan, J. Phys. Chem. C 115 (2011) p.902.
[93] S.H. Szczepankiewicz, J.A. Moss and M.R. Hoffmann, J. Phys. Chem. B 106 (2002) p.2922.
[94] A. Yamakata, T.-A. Ishibashi and H. Onishi, Chem. Phys. Lett. 333 (2001) p.271.
[95] K. Takeshita, A. Yamakata, T.-A. Ishibashi, H. Onishi, K. Nishijima and T. Ohno, J. Photoch. Photobio. A 177 (2006) p.269.
[96] C. Di Valentin and A. Selloni, J. Phys. Chem. Lett. 2 (2011) p.2223.
[97] P. Deák, B. Aradi and T. Frauenheim, Phys. Rev. B 92 (2015) p.045204.
[98] J.B. Hansen and P.E. Højlund Nielsen, *Methanol synthesis*, in G.Ertl, H.Knözinger, F.Schüth and J. Weitkamp, eds., *Handbook of Heterogeneous Catalysis*, 2nd ed., Wiley-VCH Verlag GmbH & Co. KGaA, Weinheim, 2008, p.2920–2949.
[99] H. Wilmer, M. Kurtz, K.V. Klementiev, O.P. Tkachenko, W. Grünert, O. Hinrichsen, A. Birkner, S. Rabe, K. Merz, M. Driess, C. Wöll and M. Muhler, Phys. Chem. Chem. Phys. 5 (2003) p.4736.
[100] G.L. Griffin and J.T. Yates, J. Chem. Phys. 77 (1982) p.3751.
[101] D. Scarano, G. Spoto, S. Bordiga, A. Zecchina and C. Lamberti, Surf. Sci. 276 (1992) p.281.
[102] R.R. Gay, M.H. Nodine, V.E. Henrich, H.J. Zeiger and E.I. Solomon, J. Am. Chem. Soc. 102 (1980) p.6752.
[103] B. Meyer and D. Marx, J. Phys. Condens. Matter 15 (2003) p.L89.
[104] Y. Wang, X. Xia, A. Urban, H. Qiu, J. Strunk, B. Meyer, M. Muhler and C. Wöll, Angew. Chem. Int. Ed. 46 (2007) p.7315.
[105] V. Schott, H. Oberhofer, A. Birkner, M. Xu, Y. Wang, M. Muhler, K. Reuter and C. Wöll, Angew. Chem. Int. Ed. 52 (2013) p.11925.
[106] B. Meyer and D. Marx, Phys. Rev. B 67 (2003) p.035403.
[107] H. Noei, C. Wöll, M. Muhler and Y. Wang, Appl. Catal. A. 391 (2011) p.31.
[108] A.A. Tsyganenko, L.A. Denisenko, S.M. Zverev and V.N. Filimonov, J. Catal. 94 (1985) p.10.
[109] A. Zecchina, D. Scarano and A. Reller, J. Chem. Soc. Faraday Trans. 84(7) (1988) p.2327.
[110] J. Wang, Y. Wang and K. Jacobi, Surf. Sci. 482–485 (2001) p.153.
[111] K. Hadjiivanov, B.M. Reddy and H. Knözinger, Appl. Catal. A 188 (1999) p.355.
[112] G.D. Mahan and A.A. Lucas, J. Chem. Phys. 68 (1978) p.1344.
[113] B.N.J. Persson and R. Ryberg, Phys. Rev. B 24 (1981) p.6954.
[114] R.M. Hammaker, S.A. Francis and R.P. Eischens, Spectrochim. Acta 21 (1965) p.1295.

[115] D. Scarano, S. Bertarione, G. Spoto, A. Zecchina and C. Otero Areán, Thin Solid Films 400 (2001) p.50.
[116] H. Noei, C. Wöll, M. Muhler and Y. Wang, J. Phys. Chem. 115 (2011) p.908.
[117] K. Kotsis, D. Stodt, V. Staemmler, R. Kovacik, B. Meyer, F. Traeger, D. Langenberg, T. Strunskus, M. Kunat and C. Wöll, Z. Phys. Chem. 222 (2008) p.891.
[118] W.N. Hansen, Symp. Faraday Soc. 4 (1970) p.27.
[119] J.A. Mielczarski and R.H. Yoon, J. Phys. Chem. 93 (1989) p.2034.
[120] S. Reiß, H. Krumm, A. Niklewski, V. Staemmler and C. Wöll, J. Chem. Phys. 116 (2002) p.7704.
[121] P. Rahe, M. Nimmrich, A. Nefedov, M. Naboka, C. Wöll and A. Kühnle, J. Phys. Chem. C 113 (2009) p.17471.
[122] W. Zhang, A. Nefedov, M. Naboka, L. Cao and C. Wöll, Phys. Chem. Chem. Phys. 14 (2012) p.10125.
[123] G.D. Smith and R.A. Palmer, *Fast time-resolved mid-infrared spectroscopy using an interferometer*, in *Handbook of Vibrational Spectroscopy*, J.M. Chalmers and P.R. Griffiths, eds., John Wiley & Sons, Chichester, 2002, p.625–640.
[124] M. Diem, *Modern Vibrational Spectroscopy and Micro-spectroscopy*, John Wiley & Sons, Chichester, 2015, p.167–176.
[125] H. Sezen, H. Shang, F. Bebensee, C. Yang, M. Buchholz, A. Nefedov, S. Heissler, C. Carbogno, M. Scheffler, P. Rinke and C. Wöll, Nat. commun. 6 (2015) p.6901.
[126] T. Montini, M. Melchionna, M. Monai and P. Fornasiero, Chem. Rev. 116 (2016) p.5987.
[127] , A. Trovarelli and P. Fornasiero, eds., *Catalysis by Ceria and Related Materials*, 2nd ed., Imperial College Press, London, 2013.
[128] J. Paier, C. Penschke and J. Sauer, Chem. Rev. 113 (2013) p.3949.
[129] D.R. Mullins, Surf. Sci. Rep. 70 (2015) p.42.